Mineralium Deposita
https://doi.org/10.1007/s00126-025-01364-w

ARTICLE

Cobalt-rich diagenetic Mn-oxide mineralization in the Neogene onshore Pisco Basin, Peru

Ivana C. Carcamo-Valencia[1] · Lisard Torró[1] · Johan S. Ramírez-Briones[1] · Luis Ayala[1] · Joaquín A. Proenza[2] · Thomas Aiglsperger[3] · Patrice Baby[1,4]

Received: 8 September 2024 / Accepted: 26 March 2025

Abstract

Sedimentary basin-hosted manganese oxides may represent an important yet underexplored source of critical metals. Here we present a stratigraphic, textural, mineralogical, and compositional characterization of Mn-oxide nodules, coatings, and veins in the Pisco onshore forearc basin, Peru. The Mn-oxide mineralization is stratabound within marine sandstone, siltstone, and tuff from the Neogene Chilcatay and Pisco formations. X-ray diffraction and electron microprobe analyses identify the Mn oxides as cryptomelane (± hollandite) and todorokite, which cement detrital grains and fossilize biological remains. Bulk chemical analyses of nodules, coatings, and veins reveal significant cobalt enrichment (mean = 0.17 ± 0.15 wt% Co; up to 0.63 wt% Co), corroborated by electron probe microanalysis of individual Mn oxide phases (mean = 0.37 ± 0.33 wt% Co; up to 2.1 wt% Co). The stratigraphic control, biomorphic replacement, mineralogy, and chemical composition collectively indicate a diagenetic origin for the Mn-oxide mineralization. The formation pathway likely involved organic matter decay or brine-hydrocarbon interactions coupled with Mn and Fe reduction, resulting in metal-enriched porewaters that circulated along structures and permeable horizons. Subsequent precipitation under oxygenated conditions occurred during late Pliocene uplift and exposure of the East Pisco Basin. This study demonstrates that diagenetic Mn oxides exposed in onshore basins represent a potential resource for manganese and critical elements such as cobalt.

Introduction

Ferro-manganese-oxide crusts and nodules in the seabed have gained recognition as potential future resources for high- and green-tech metals since the 1960s, when John L. Mero predicted their potential as an essentially endless supply of Mn, Co, Ni, and Cu (Hein et al. 2000, 2013, 2020; Hein and Koschinsky 2014; Lusty and Murton 2018; Lusty et al. 2018; García et al. 2020). Fe-Mn crusts are found on seamounts, ridges, and uplifts throughout ocean basins (e.g., Pacific, Hein et al. 2000; Atlantic, Josso et al. 2019; Benites et al. 2020; Indian, Banakar et al. 1997; Arctic, Hein et al. 2017; Konstantinova et al. 2017), while Fe-Mn nodules typically form on sediment-covered abyssal plains at depths of 4,000–6,500 m, particularly where sedimentation rates are low (< 10 mm kyr^{-1}; Hein and Koschinsky 2014; Hein et al. 2020). Shallow-water (< 100 m) nodules are rare but known in a few locations such as the Baltic Sea (Hein and Koschinsky 2014), the Kara Sea (Vereshchagin et al. 2019; Shulga et al. 2022), and the Chukchi and East Siberian seas (Baturin and Dubinchuk 2011).

Fe-Mn crusts primarily form through hydrogenetic precipitation, whereas nodules may form through either hydrogenetic or diagenetic processes (Hein et al. 2000; Hein and Koschinsky 2014). Hydrogenetic precipitation involves direct oxidation of Mn^{2+} and Fe^{2+} from cold seawater and subsequent accretion of Mn^{4+} and Fe^{3+} oxide colloids onto rock substrates (crusts) or around a nucleus (nodules). Hydrogenetic Fe-Mn oxides typically contain Fe-rich vernadite (δ-MnO_2) and X-ray amorphous Fe oxyhydroxide

Editorial handling: B. Lehmann

✉ Lisard Torró
lisardtorro@hotmail.com

[1] Geological Engineering Program, Pontifical Catholic University of Peru (PUCP), San Miguel, Lima 15088, Peru

[2] Departament de Mineralogia, Petrologia i Geologia Aplicada, Universitat de Barcelona, Barcelona 08028, Spain

[3] Department of Civil Engineering and Natural Resources, Luleå University of Technology, Luleå 97187, Sweden

[4] Géosciences Environnement Toulouse, Université de Toulouse, CNES, CNRS, IRD, UPS, Toulouse 31400, France

(feroxyhyte, δ-FeOOH), Mn/Fe ratios near 1, with enrichment in Co (up to 0.38 wt%), Te, Ce, and Pt. In contrast, diagenetic precipitation occurs from sediment porewater, which is essentially chemically modified ocean water. It produces nodules composed of 10 Å manganates (buserite, todorokite, asbolan), 7 Å manganates (birnessite), and Fe oxyhydroxides (goethite and the X-ray amorphous feroxyhyte and ferrihydrite) accreted around a hard nucleus. Diagenetic nodules typically show high Mn/Fe ratios (> 10) and high contents of Ni (up to 1.30 wt%), Cu (up to 1.07 wt%), and Li (up to 311 ppm; Hein et al. 2000; Hein and Koschinsky 2014). Finally, hydrothermal Fe-Mn oxide precipitates in crusts or stratabound mineralization show variable Mn/Fe and metal contents depending on their geodynamic setting (Glasby 1988; Josso et al. 2017; Pelleter et al. 2017; Zhou et al. 2022) with todorokite as the predominant manganese phase (Hein et al. 2000).

Within the Chilean and Peruvian Exclusive Economic Zones (EEZ; Fig. 1), significant marine resources of Mn-oxide nodules have been identified with valuable metal enrichment. Data compiled by García et al. (2020) and Toro et al. (2020) reveal Mn nodules in the Chilean EEZ with notable Co contents (e.g., 0.16–0.53 wt% in southern Chile at depths of ~ 3,800 - 4,000 m), while those in the Peru Basin, located 3,000 km offshore at depths of 3,900 - 4,300 m, show high Ni (up to 1.30 wt%) and Li (up to 311 ppm; Glasby 2013; Hein and Koschinsky 2014; Toro et al. 2020). Although these resources represent significant economic potential for the region, their exploitation remains challenging due to persistent political uncertainties and environmental concerns regarding seabed habitat disruption (Boschen et al. 2013; Sparenberg 2019; Hein et al. 2020; Cunningham 2022; Helmons et al. 2022; Katona et al. 2022). These challenges make it likely that accessible onshore resources will remain critical for meeting mineral demands in the foreseeable future.

Onshore Mn-oxide mineralization along the Pacific coast of South America presents an attractive alternative to seafloor deposits. In north-central Chile, discoidal, spherical, and bulbous Mn nodules of diagenetic origin occur within silty mudstone of the Miocene Bahía Inglesa Formation (Fig. 1; Achurra et al. 2009). These Mn nodules are composed of todorokite and trace amounts of cryptomelane, which act as a cement for silicate minerals and siliceous microorganisms (e.g., diatoms), and contain relatively low cobalt (< 0.05 wt% Co). Similar onshore manganese nodules occur on the Peruvian coast, particularly in the East Pisco Basin (Fig. 1). In this region, Bessler (1975) conducted an exploratory study of Mn nodules hosted in diatomite horizons of the Pisco Formation (Ica region; 14°22'S, 75°37'W), reporting mean Ni and Co contents of 0.12 wt% and 0.11 wt%, respectively (n = 5). During a routine geological field camp with Geology students, we discovered abundant Mn oxide nodules, veins, and coatings in another location within the East Pisco Basin—the largely underexplored Rio Grande Valley. Building upon Bessler's (1975) preliminary findings, we have conducted a comprehensive study of these Mn oxides to assess their origin and economic potential.

Geological setting

Cenozoic forearc basins of the Peruvian margin

The tectonic regime of the Peruvian margin is controlled by the oblique subduction of the Nazca/Farallon Plate underneath the South American Plate along the Peru-Chile Trench since Cretaceous times (Di Celma et al. 2017). The Nazca Ridge, a bathymetric high delineated by multiple seamounts (Casalbore 2018), has been subducted beneath the South American Plate since at least the end of the middle Miocene (~ 11.2 Ma) and interacts with the active convergent margin enhancing tectonic erosion (Hampel 2002; Clift et al. 2003). Another significant geological feature at the latitudes of the study area is the Nazca Drift System, which extends from the southwest of the Nazca Ridge to the Peru-Chile Trench at water depths between 2,090 and 5,330 m above the abyssal basins of Peru and Chile (Fig. 1). It stands as the largest abyssal drift system of the Pacific Ocean (Calvès et al. 2022).

Two persistent structural ridges, the Outer Shelf High and the Upper Slope Rise, have exerted a controlling influence on the geometry and distribution of Cenozoic forearc basins along the Peruvian continental margin. These include the Talara, Sechura, Salaverry, Trujillo, Lima, Pisco, Moquegua, and Mollendo basins (Fig. 2A; Thornburg and Kulm 1981). The Eocene to Pliocene Pisco Basin, which extends from 13° to 15° S (León et al. 2008; Di Celma et al. 2016; Viveen and Schlunegger 2018), is part of the central and southern portions of the Peruvian forearc that were influenced by the passage of the aseismic Nazca Ridge since ~ 4–5 Ma (Macharé and Ortlieb 1992; Hampel 2002; Espurt et al. 2007; George et al. 2022). The Pisco Basin is divided into two sub-basins, West Pisco and East Pisco, which are separated by the Outer Shelf High (Fig. 2A; Thornburg and Kulm 1981; Quispe et al. 2018) probably since the late Oligocene (Ochoa et al. 2021).

The East Pisco Basin, where the study area is located, corresponds to the onshore portion of the basin (Fig. 2; Gioncada et al. 2018; Di Celma et al. 2022) and is interpreted as a semi-enclosed, shallow embayment (Di Celma et al. 2016). The sedimentary fill of the East Pisco Basin is divided into two megasequences by Di Celma et al.

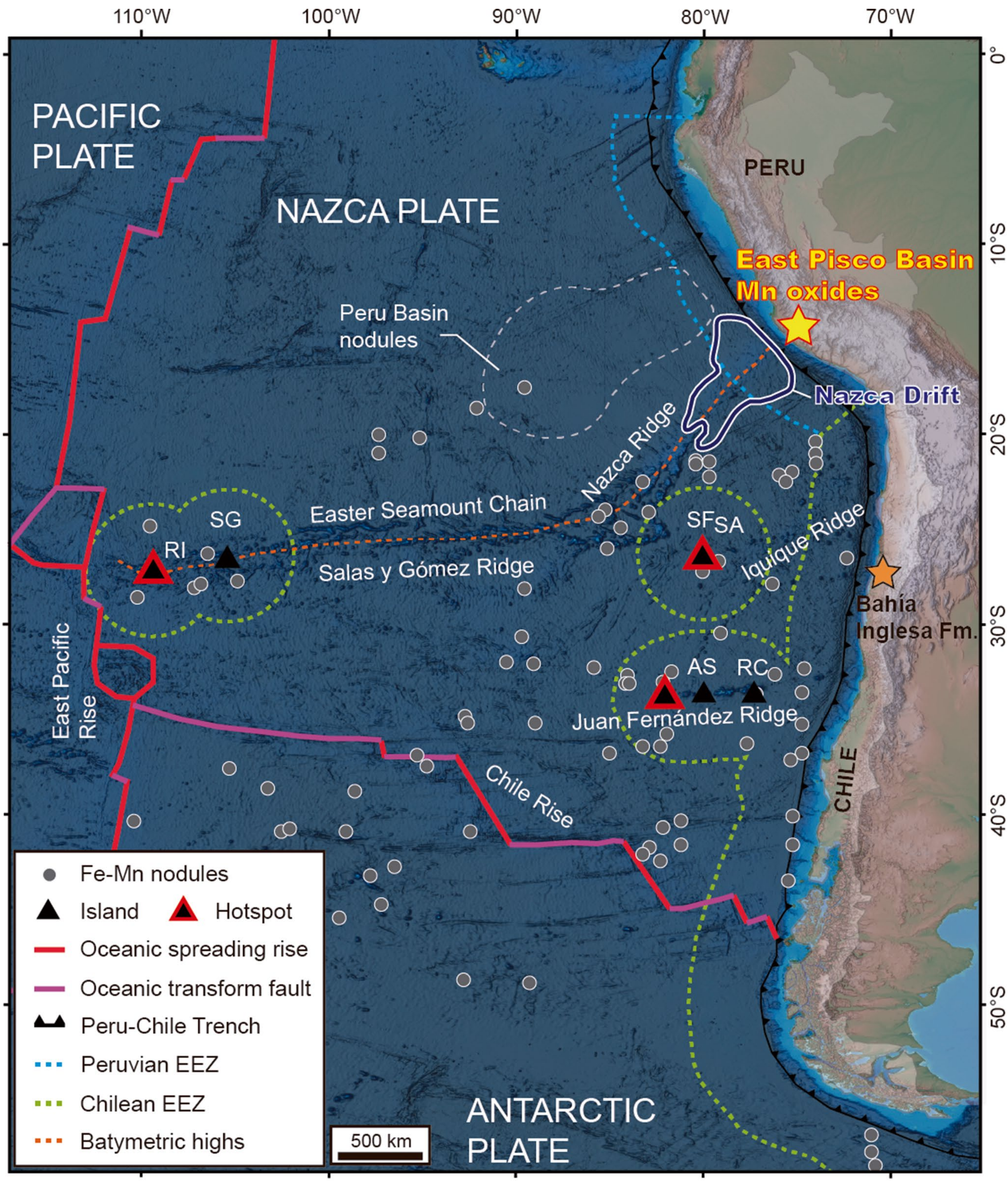

Fig. 1 Location of (Fe-)Mn oxide nodule fields in the Chilean and Peruvian Exclusive Economic Zones (EEZ; circles) and onshore descriptions (stars). Adapted from García et al. (2020) and Toro et al. (2020). Delimitation of Nazca Ridge and Nazca Drift from Calvès et al. (2022). Global elevation and bathymetry from the National Centers for Environmental Information (2022). Abbreviations: RC—Robinson Crusoe Island; SF—San Félix Island; SA—San Ambrosio Island; RI—Rapanui Island; SG—Salas y Gómez Island; AS—Alejandro Selkirk Island

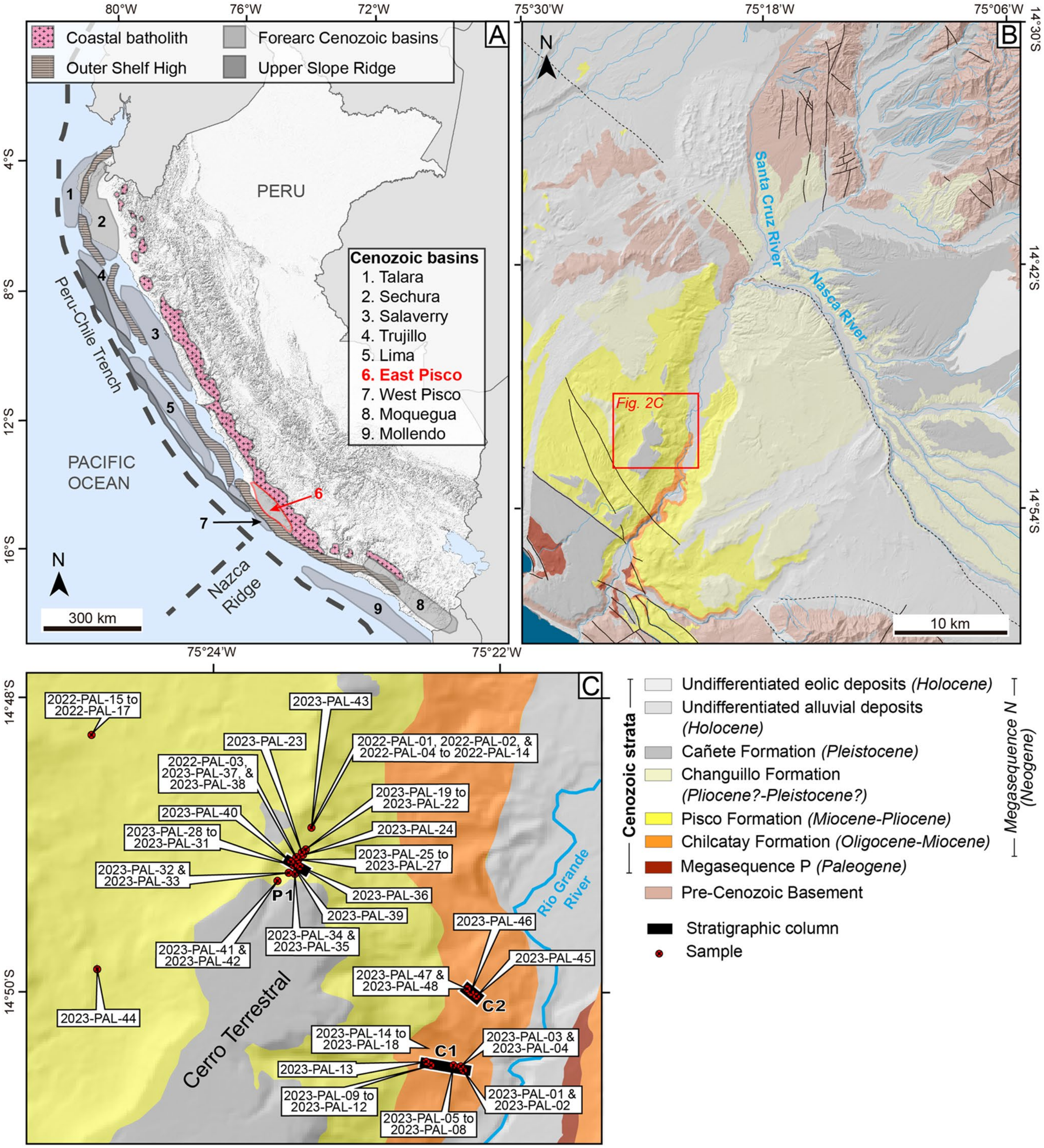

Fig. 2 Geological framework of the studied Mn oxides in the Chilcatay and Pisco formations, East Pisco Basin. **A** Major Cenozoic forearc basins along the Peruvian margin. The Coastal Cordillera is traced offshore as the Outer Shelf High. Modified from Thornburg and Kulm (1981) and Ochoa et al. (2021). **B** Regional geological map of the Rio Grande Valley (modified from León and Torres 2003). The red rectangle indicates the location of the study area. **C** Geological map of the study area indicating the position of samples (labels in white boxes) and stratigraphic columns (C1, C2, and P1). The geology base map has been modified from León and Torres (2003) according to our own field observations. Digital Elevation Model (DEM) provided by the European Space Agency (2024)

(2022), namely the megasequence P (Paleogene) and the megasequence N (Neogene). These megasequences overlie a deformed and heterogeneous pre-Cenozoic basement, which includes Paleozoic to Mesozoic intrusive, Jurassic volcano-sedimentary, and Proterozoic metamorphic rocks (León et al. 2008; Di Celma et al. 2017). The megasequence P consists of middle Eocene to lower Oligocene sedimentary successions, including medium- to coarse-grained bioclastic sandstone that stratigraphically pass upward into siltstone. The megasequence N is composed of uppermost Oligocene to Pliocene bioclastic sandstone and siltstone of the Chilcatay Formation, and fossiliferous sandstone and conglomerate, and diatomaceous and tuffaceous siltstone of the Pisco formation (Dunbar et al. 1990; León et al. 2008; Di Celma et al. 2022; Malinverno et al. 2025). The clastic sequences in both the Chilcatay and Pisco formations have been interpreted as a succession of transgressive depositional sequences (Di Celma et al. 2018a, b, 2019). The East Pisco Basin is capped by Quaternary conglomerate deposits of the Cañete Formation (León et al. 2008; Ochoa et al. 2021).

The structural framework of the East Pisco Basin exhibits numerous, predominantly NW–oriented normal faults and rotated blocks associated with grabens and semi-grabens (Macharé 1987; Rustichelli et al. 2016; Viveen and Schlunegger 2018). The tectonic regime under which the East Pisco Basin was formed is not totally defined yet. Some authors state alternating phases of compression and transtensional tectonics, and prolonged subsidence during the Paleogene and Neogene, with uplift and compression occurring during the Quaternary because of the arrival of the Nazca Ridge (Clift et al. 2003; León et al. 2008; Viveen and Schlunegger 2018; Di Celma et al. 2022). In contrast, other authors suggest a continuous compressional regime from the late Oligocene to the Quaternary associated with Andean shortening (Quispe et al. 2018; Ochoa et al. 2021).

The Chilcatay and Pisco formations

The studied Mn oxides are hosted by the Chilcatay and Pisco formations in the East Pisco Basin. The Late Oligocene to Early Miocene Chilcatay Formation (DeVries and Jud 2018) consists predominantly of basal massive sandstone and large boulders of pre-Cenozoic basement rocks, followed by marine diatomaceous and tuffaceous sandy siltstone (Di Celma et al. 2018a). In the study area (i.e., left side of the Río Grande Valley, in the surroundings of Cerro Terrestral), the Chilcatay Formation is only exposed at the valley sides and bottom, with a variable thickness ranging from 150 to 320 m (Fig. 2B). In this area, it consists of bioturbated and fossiliferous calcareous sandstone interbedded with coarse-grained sandstone, conglomerate, biogenic mudstone, and siltstone (León et al. 2008).

The Mio-Pliocene Pisco Formation (Ochoa et al. 2021) is one of the main lithostratigraphic units of the East Pisco Basin, with a variable thickness between 200 and 1,000 m (Dunbar et al. 1990; León et al. 2008; Di Celma et al. 2018b). This marine formation mainly consists of sandstone, siltstone, and diatomite, along with minor amounts of tuff and dolomite, the latter of which contains an outstanding collection of vertebrate fossil fauna (Di Celma et al. 2016; Ochoa et al. 2021; Malinverno et al. 2025). Tuffaceous diatomite and tuff correspond to the Nazca volcanic event (Di Celma et al. 2016). The Pisco Formation covers most of the study area (Fig. 2B), where it has a thickness of 370 m and unconformably overlies the Chilcatay Formation and underlies Quaternary deposits of the Cañete Formation (León et al. 2008; Ochoa et al. 2021). Within the study area, the Pisco Formation consists predominantly of brownish- to reddish-grey diatomaceous biogenic mudstone interbedded with fine- to coarse-grained sandstone, conglomerate, fossiliferous beds, tuff, and sporadic dolomite, calcareous concretions, and phosphatic beds (León et al. 2008; Bosio et al. 2024).

Sampling and analytical methods

This study is based on 65 representative Mn oxide surface samples including nodules, veins, and coatings collected from the Rio Grande Valley near the town of Palpa (Ica Region, southern Peru). It should be noted that all geochemical data presented in this study derive from selective sampling of Mn-bearing features (nodules, veins, and crusts) rather than bulk rock analysis. Samples were specifically targeted to characterize the nature and composition of the Mn oxide mineralization itself, not to determine average grades of the host rock succession. A list of individual hand-sample descriptions and sampling locations is provided in the Electronic Supplementary Material (ESM) Table S1. The location of the samples is illustrated in Fig. 2C. The stratigraphic position of the Mn-oxide samples under investigation is contextualized within the framework of three stratigraphic columns, which have been produced as part of this research. The stratigraphic columns cover segments of the Chilcatay (columns C1 and C2) and Pisco (column P1) formations in the surroundings of Cerro Terrestral and show in detail the lithology, granulometry, and sedimentary structures (Fig. 3). The stratigraphic columns, key field pictures, and descriptions of the different stratigraphic levels, including the sampling sites, are provided in ESM.

A complete characterization of the chemical composition of the Mn oxides was performed at ALS Vancouver using

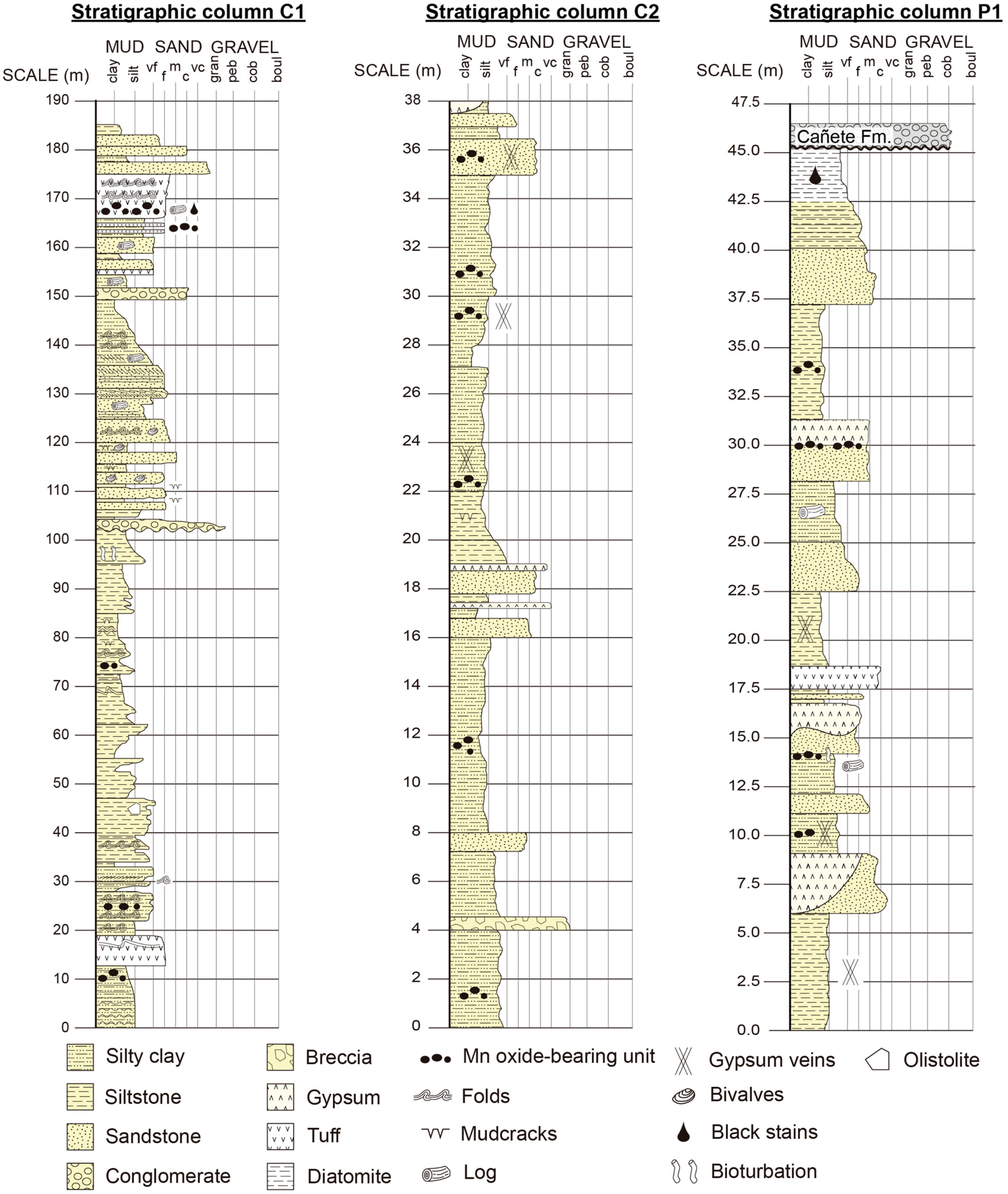

Fig. 3 Stratigraphic columns covering segments of the Chilcatay (C1 and C2) and Pisco (P1) formations in the Río Grande Valley, East Pisco Basin, hosting the studied Mn-oxide mineralization. The location of the areas covered by the columns is provided in Fig. 2C

the analytical packages ME-XRF26 s and CCP-PKG01. The package ME-XRF26 s is designed for chromite and manganese ores and is suitable for the determination of major and minor elements in mineralized samples that require a high dilution digest. The samples were fused with lithium metaborate flux and then poured into a platinum mold. The resultant fused disks were analyzed by X-ray fluorescence (XRF) spectrometry. This method also included LOI calculation at 1,000 °C. The package CCP-PKG01 comprises five methods: (i) major elements by ICP-AES analysis following a combination of fusion and acid digestion plus LOI calculation by furnace or thermogravimetric analyzer; (ii) trace elements by ICP-MS analysis following a combination of fusion and acid digestion; (iii) total carbon and sulfur by induction furnace/IR; (iv) base metals by ICP-AES analysis following a four-acid digestion; and (v) volatile trace elements by ICP-MS analysis following an aqua-regia digestion. A full dataset of whole-rock chemical compositions of the analyzed samples is available in ESM Table S2.

The elemental composition of nodules was mapped through micro-X-ray fluorescence (µXRF) using a Bruker M4 TORANDO fast mapping instrument at Luleå University of Technology, operating under a vacuum of 2 mbar at 50 kV and 600 ìA with a rhodium anode tube. Pixels were achieved via a 50 ìm step size, and measurements were performed applying a 20 ìm spot size. The spectral acquisition and data treatment were both performed using the M4 TORNADO software from Bruker.

The major mineralogy of the Mn oxides was analyzed through X-ray diffraction (XRD). For XRD analysis, the samples were crushed and then manually ground in an agate mortar and pestle to obtain a very fine powdered material <35 µm. The powdered material was pressed using a glass plate to obtain a flat surface in cylindrical standard sample holders of 16 mm in diameter and 2.5 mm in height. XRD data were collected with a Bruker D8 Discover diffractometer in Bragg-Brentano $\theta/2\theta$ geometry of 240 mm of radius at the *Centro de Caracterización de Materiales* at PUCP (CAM-PUCP). Scanning from 4 to 80 ° (2θ) was performed at a step size of 0.039° and a scan time of 4 s per step. Nickel filtered Cu Kα radiation (k = 1.5418 Å) and 40 kV–40 mA conditions were used. The software PANalytical X'Pert Highscore 2.0.1 was used to subtract the background of the patterns, detect the peaks, and assign mineral phases to each peak.

Fourteen polished thick sections and three polished thin sections were prepared for petrographic and electron probe microanalysis (EPMA). The petrography was performed using transmitted and reflected light in a Zeiss Primotech polarizing microscope. Major and minor element analyses of Mn-oxide minerals were performed at the *Centres Científics i Tecnológics de la Universitat de Barcelona* (CCiTUB) using a JEOL JXA- 8230 electron microprobe equipped with five wavelength-dispersive spectrometer (WDS) detectors. The accelerating voltage was set to 15 kV, with a beam current of 15 nA, and a beam diameter of 1 µm. The analyses were performed using the following natural and synthetic standards and lines: diopside (Si, Kα), kyanite (Al, Kα), wollastonite (Ca, Kα), orthoclase (K, Kα), galena (Pb, Mα), barite (Ba, Lα; S, Kα), apatite (P, Kα), periclase (Mg, Kα), albite (Na, Kα), rhodonite (Mn, Kα), hematite (Fe, Kα), metallic Co (Co, Kα), sphalerite (Zn, Kα), cuprite (Cu, Kα), bunsenite (Ni, Kα), and rutile (Ti, Kα). The detection limits (d.l.) for each element were 500 ppm Si, 350 ppm Al, 600 ppm Ca, 450 ppm K, 1,500 ppm Pb, 900 ppm S, 1,000 ppm P, 500 ppm Mg, 550 ppm Na, 800 ppm Mn, 700 ppm Fe, 650 ppm Co, 1,350 ppm Zn, 950 ppm Cu, 725 ppm Ni, 850 ppm Ti, and 1,500 ppm Ba. The chemical composition of analyzed minerals is reported in ESM Table S3.

Results

Stratigraphic position and facies of Mn oxides

The segments of the Chilcatay and Pisco formations with the Mn-oxide mineralization are predominantly composed of clastic material, including interbedded sandstone, siltstone, and silty clay, as well as more restricted tuff horizons (Fig. 3 and ESM). Additionally, massive gypsum beds are also present in both formations, with thicknesses ranging from a few centimeters to ~3 m. Centimeter-scale nodular gypsum is observed in sandstone layers of the Chilcatay Formation, while in the studied segment of the Pisco Formation, some of the gypsum beds change laterally to sandstone. A noteworthy feature also observed in the stratigraphic column in the Pisco Formation is the presence of a ~10 m-thick diatomite bed with a distinctive bright creamy color at the top of the sequence. Fibrous gypsum veins, measuring between 1 mm and 20 cm in thickness, crosscut the stratigraphic series with a predominant NW orientation, while an associated secondary set of gypsum veins exhibits a NE orientation. Additionally, specific strata of both formations exhibit a high fossiliferous content, comprising primarily bivalves, logs, and ichnofossils. Local oily black stains in some rocks are potentially linked to liquid hydrocarbon flow.

Mn-oxide mineralization in the Rio Grande Valley occurs primarily as nodules, concretions, veins, surface coatings, and less frequently as fossil replacements and massive lenses (Figs. 4 and 5). Nodules and concretions concentrate along specific stratigraphic levels of sandstone, siltstone, and tuff (Figs. 3 and 4B-D). In the Pisco Formation, grape-shaped composite Mn-oxide nodules hang from sedimentary gypsum bed contacts (Fig. 4E). Nodule abundance

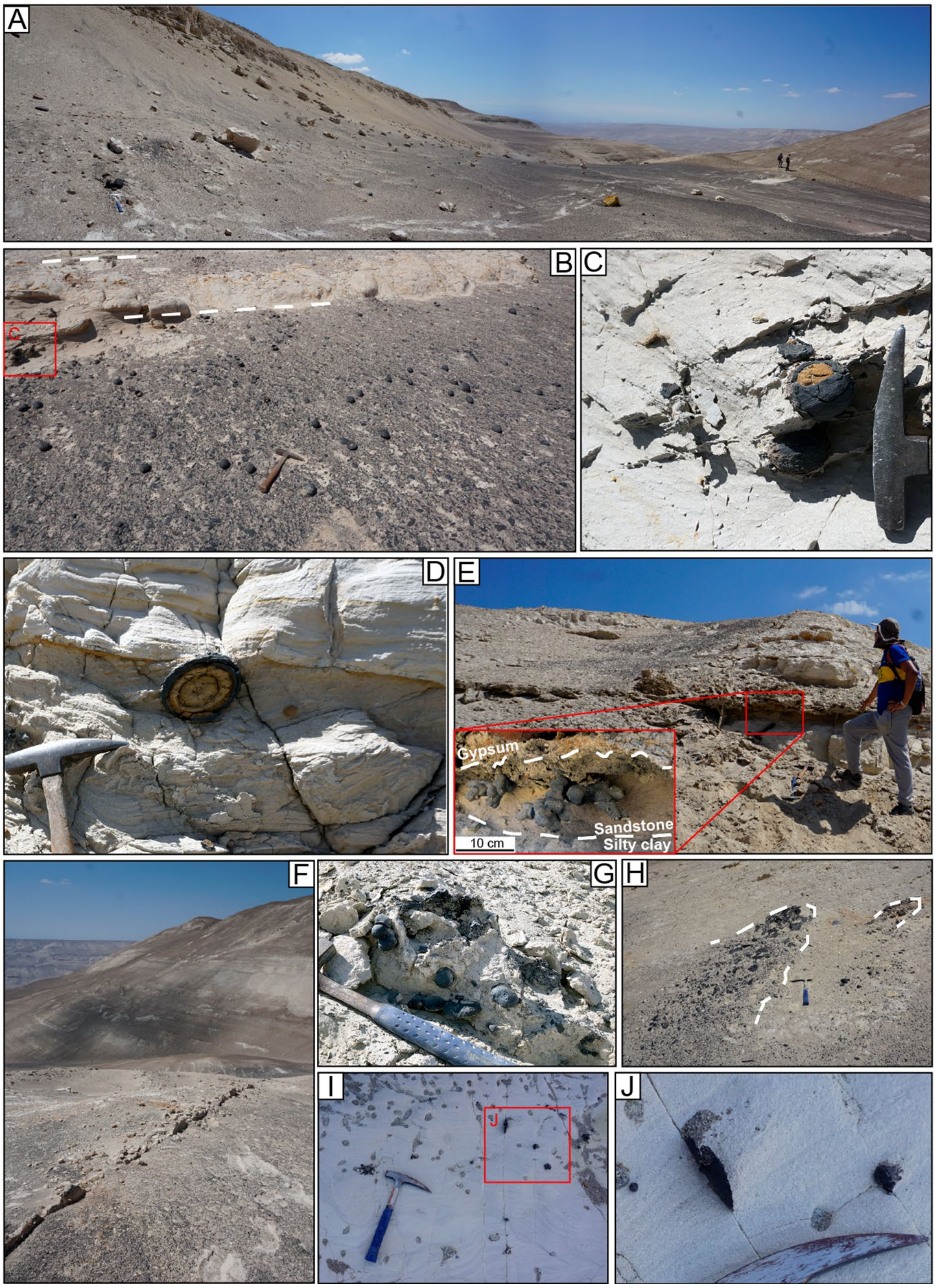

Fig. 4 Field view of the Mn-oxide mineralization in the Río Grande Valley, East Pisco Basin. **A** General view of the valley floor covered by a dark stone pavement with abundant Mn-oxide nodules and fragments; Pisco Formation strata are very poorly exposed in the hillsides. **B** Detail of stone pavement comprising cm-scale nodules, concretions, and fragments in the valley floor and exposure of Chilcatay Formation strata with in situ Mn oxide-nodules in the hillside. **C** Detail of spherical Mn-oxide nodules in sandstone of the Chilcatay Formation. **D** Detail of a freshly cut Mn-oxide nodule hosted in sandstone of the Chilcatay Formation showing concentric structure. **E** General view of an outcrop of the Pisco Formation consisting of medium-grained sandstone overlain by a gypsum bed. “Grape-like” Mn-oxide concretions are at the contact between these lithologies. **F** A straight gypsum vein protrudes over siltstone bedrock of the Pisco Formation. **G** Close-up of the gypsum vein with accreted cm-scale Mn-oxide nodules. **H** Manganese-oxide nodules and fragments in a chimney-like structure. **I** Botryoidal Mn-oxide nodules and Mn-oxide veins in tuff of the Chilcatay Formation. **J** Close-up view of the Mn-oxide veins and botryoidal nodules in tuff; note also the voids left by eroded nodules

varies laterally, with concentrations increasing near feeder structures. Furthermore, manganese-oxide nodules and concretions occur accreted onto or cemented within continuous gypsum veins (≤ 10 cm thick) that protrude from the clastic bedrock (Fig. 4F, G). They also accumulate around chimney-like structures, which in the field appear as small, circular mounds protruding from the surface and displaying distinct ochre coloration (Fig. 4H). Fragments of Mn-oxide nodules in valley bottom stone pavements (see McFadden et al. 1987; Cooke et al. 2006) create distinctive black surface colorations (Fig. 4A, B).

Nodules exhibit diverse morphologies: spheroidal (Fig. 5A), ellipsoidal (Fig. 5B, F), discoidal (Fig. 5C, D), or irregular (Fig. 5G). They may form composite bulbous (Fig. 5C), lobate rod (Fig. 5H), and grape-like aggregates (Fig. 4E). Sizes range from millimetric micronodules to 15 cm diameter specimens. Nodule surfaces may be botryoidal with slight luster (Fig. 5C, D), sandy (Fig. 5A), or rough matt (Fig. 5B). In places, manganese oxides appear as dendrites as well as small (< 3 mm) dark specks transitioning to incipient micronodular forms, occurring as fillings and replacements in white mudstone and siltstone (Fig. 5I).

Cross-sections of massive Mn-oxide nodules reveal septarian structures with open or gypsum-filled cracks (Figs. 5E, 6 and 7A). Freshly cut surfaces show abundant fine-grained detrital particles embedded in the Mn oxides (Fig. 7A, B). Some nodules display black Mn-oxide rinds surrounding ochre sandstone cores (Fig. 4C, D) or dark brownish sandstone mantles that surround brighter ochre sandstone cores (Fig. 7A). One sample shows a black Mn-oxide rind encapsulating an irregular, deformed white sandstone core, with thin Mn oxide veinlets traversing the core to connect opposite sides of the Mn encasement (Fig. 5F).

Mn-oxide coatings form non-continuous, irregular accretions on siltstone, silty clay, and tuffaceous silty clay. Their surfaces exhibit rough, sandy (Fig. 5K), or smooth textures, with thicknesses from millimeters to 7 cm. Mn-oxide veins are massive, continuous structures (1 mm–1.2 cm thick) forming straight linear arrangements that cut across bedding and protrude from the bedrock (Fig. 4I, J), occasionally transitioning abruptly to nodules. Some veins display botryoidal surfaces (Fig. 5J).

Rare massive Mn-oxide lenses (≤ 10 cm thick) form along contacts between permeable and overlying impermeable beds (Fig. 5L). In isolated cases, Mn oxides replace ichnofossils, as in a 7 cm-thick Mn oxide lens containing elliptical burrows fossilized by Mn oxides (Fig. 5M). Elsewhere, Mn oxides fossilize individual elliptical tunnels (≤ 20 cm long) featuring small bulges and crests (Fig. 5N).

Element distribution maps

Compositional maps of diametrically cut Mn-oxide nodules reveal distinct elemental distribution patterns (Figs. 6 and 7). The massive nodule in Fig. 6 shows relatively homogeneous Mn content, while Fe, Co, K, and Mg display concentric, oscillatory zoning following the nodule outline. Iron and K exhibit nearly mimetic distributions with inner mantle enrichment relative to the core and depletion in the outer mantle and rim, whereas Co shows an antithetic pattern. Magnesium contents remain relatively homogeneous except for enrichment along a thin (< 1 mm) band in the nodule mantle. The maps also reveal irregular, discontinuous thin gypsum infills along growth zones within the nodule.

Figure 7A shows elemental distribution in a nodule comprising a black Mn-oxide rind surrounding a Fe-rich, dark reddish-brown sandstone mantle and a bright ochre sandstone core. The Mn-oxide rind is enriched in Co and K, in addition to Mn, and depleted in Fe and Mg compared to the sandstone mantle and core. Gypsum occurs along the core-mantle contact and fills septarian cracks radiating around the core.

In the branching, lobate-rod aggregate shown in Fig. 7B, Mn content is relatively homogeneous, while Co and K contents vary, displaying irregular to botryoidal bands with antithetic distributions. Gypsum concentrates along the aggregate edges and internal contacts between individual nodular forms.

These elemental maps demonstrate that Co distribution is heterogeneous across nodules of different morphologies. They also highlight the intimate textural relationship between Mn oxides and gypsum, with the latter occurring as crack infills within the nodules.

Microtextures of the Mn oxides

In nodules and concretions, Mn oxides cement detrital particles with varying porosity—from cement-supported fabrics with no interparticle porosity (Fig. 8A, B) to high porosity with minor cement (Fig. 8C). Detrital grains comprise mainly angular to sub-angular quartz and plagioclase (100–200 µm) with minor mica (Fig. 8D). Tuff levels contain curviplanar juvenile glass shards up to 500 µm long (Fig. 8E). Frequent thin (< 200 µm) massive (Fig. 8F, G), fibrous, microporous, or colloidal (Fig. 8H) Mn-oxide veinlets cut across the primary nodule mass composed of detrital particles and Mn oxides cement. Several lines of evidence suggest a polycyclic nature of Mn mineralization within these nodules: (1) incorporation of sub-rounded fragments containing both Mn-oxides and detrital particles within intranodular veinlets (Fig. 8F), and (2) multiple veinlet generations exhibiting clear crosscutting relationships (Fig. 8G). Additionally, Mn oxides commonly replace biomorphic structures, including diatoms (Figs. 8H, I) and fibrous microlaminae (Fig. 8A).

Mn-oxide veins show similar microtextures, with Mn oxides cementing angular to subangular detrital grains (50–200 µm) with variable porosity occlusion (Fig. 8J). Massive Mn-oxide domains alternate with microporous zones (Fig. 8K). Manganese oxides in veins fossilized biomorphs including fibrous (vegetal?) microlaminae and diatoms (Fig. 8L). Mn-oxide coatings occur either as cement to detrital particles or as massive layers. The former shows grain-supported textures with high porosity and minor cement (Fig. 8M), while the latter forms massive or poorly porous colloidal fabrics between angular grains (Fig. 8N), sometimes displaying micro-urchin terminations (Fig. 8O).

Major and trace element (bulk) geochemistry

Table 1 summarizes the chemical compositions of Mn oxides by morphological type. Most samples show high MnO contents (> 34.3 wt%), except for six samples with abundant sedimentary material (4.85–28.7 wt% MnO). Fe_2O_3 contents are generally lower (< 9.73 wt%) than MnO, with Mn/Fe ratios ranging from 0.62 to 50.2. Variable contents

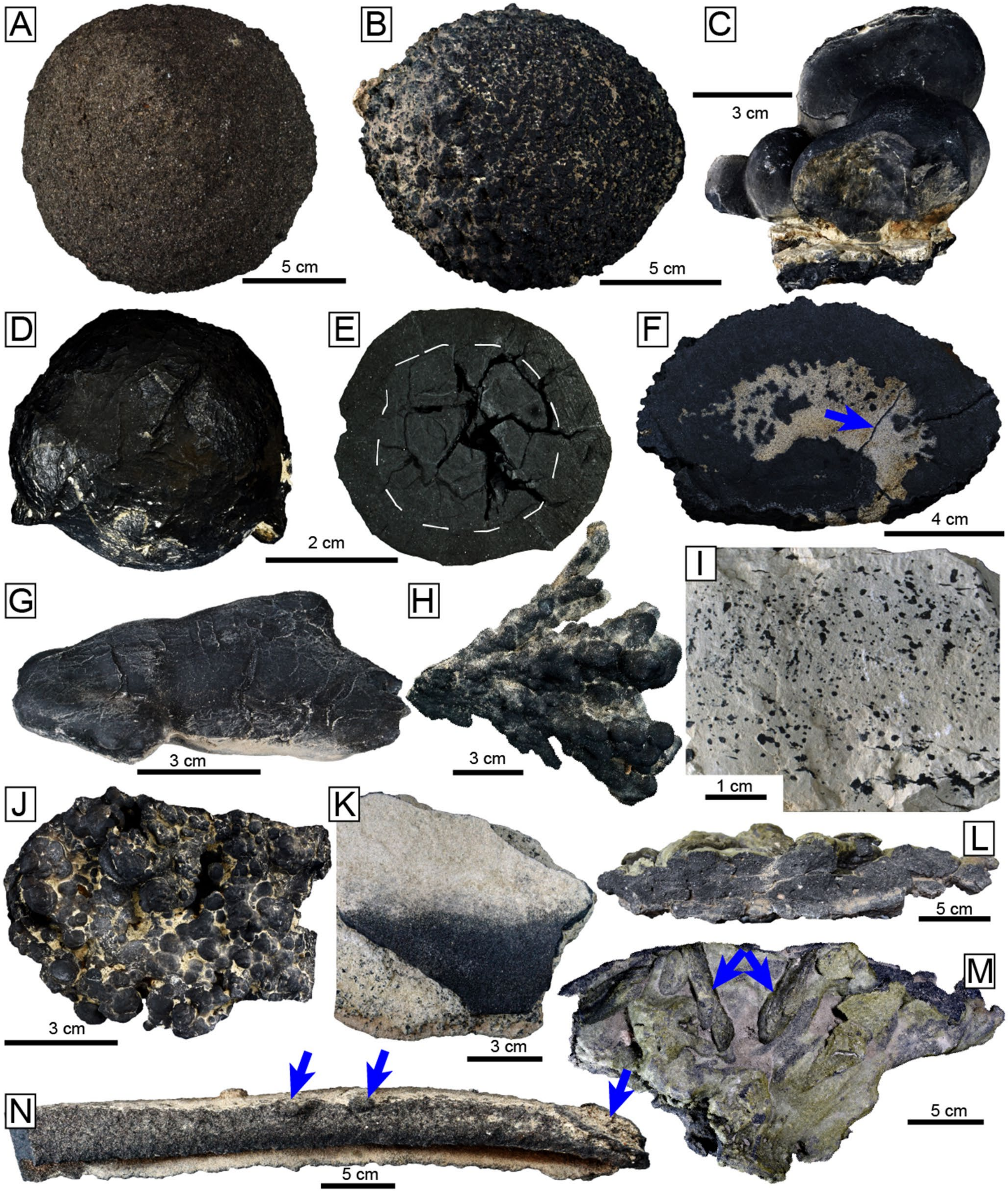

of SiO_2, P_2O_5, CaO, Na_2O, Al_2O_3, and MgO reflect detrital mineral components. LECO analysis reveals low S (mean = 0.19 wt%, up to 3.75 wt%) and C contents (mean = 0.07 wt%, up to 5.29 wt%), with elevated values correlating with gypsum/anhydrite and carbonate precipitates.

Cobalt contents range from 111 to 6,290 ppm (mean = 1,650 ± 1,486 [1σ] ppm). Other valuable metals occur in minor amounts: Zn (up to 1,330 ppm, mean = 323 ± 260 ppm), Ni (up to 1,405 ppm, mean = 140 ± 318 ppm), Cu (up to 496 ppm, mean = 137 ± 142 ppm), V (up to 736 ppm,

Fig. 5 Morphological and textural variations of the Mn-oxide mineralization in the Chilcatay and Pisco formations in the East Pisco Basin. **A** Spheroidal nodule with sandy surface [2023-PAL- 13]. **B** Ellipsoidal nodule with rough surface [2023-PAL- 34]. **C** Composite bulbous concretion on fibrous gypsum (white material); individual nodules show smooth surfaces [2022-PAL- 04]. **D** Discoidal nodule with smooth, shiny surface [2022-PAL- 10]. **E** Cross-sections of diametrically-cut Mn-oxide nodule with radial septarian cracks concentrating in the center and reducing their widths toward the outer part of the nodule (white line) [2022-PAL- 10]. **F** Complex wrapping of black Mn oxides around deformed, bright-colored sandstone; note that fragments of Mn oxides appear within the sandstone core, which is crosscut by thin Mn-oxide veinlets (arrow) [2023-PAL- 34]. **G** Irregular nodule of elongate shape [2023-PAL- 27]. **H** Branching cluster of lobate rods [2023-PAL- 36]. **I** Mn-oxide thin stringers, specks, and incipient micronodules as fillings and replacements in white mudstone [2023-PAL- 11]. **J** Manganese-oxide vein with botryoidal surface [2022-PAL- 03]. **K** Manganese-oxide coating with rough, micro-botryoidal surface [2023-PAL- 02]. **L**, **M** Massive Mn-oxide lens with a thickness of 7 cm with multiple burrows (arrows) fossilized by Mn oxides on one of its sides [LA-P12]. **N** 18-cm-long burrow with an ellipsoidal section and small, round globe-like bulges (arrows) and crests at one end of the burrow (arrow) [2023-PAL- 40]

mean = 180 ± 216 ppm), Pb (up to 784 ppm, mean = 69 ± 160 ppm), and Mo (up to 432 ppm, mean = 39 ± 125 ppm). Remaining potentially economic metals (Li, Sc, Cr, Ge, Ga, In, Te, Bi) show mean values below 25 ppm. Potentially deleterious elements exhibit variable contents: Cd (up to > 1,000 ppm (i.e., higher than upper detection limit), mean = 120 ± 280 ppm), As (up to > 250 ppm, mean = 142 ± 81 ppm), Tl (up to > 250 ppm, mean = 44 ± 68 ppm), and Sb (up to 27 ppm, mean = 3 ± 7 ppm).

REY (lanthanides + Y) contents are generally low (mean ΣREY = 121 ppm). Individual REE values are typically < 30 ppm, except for Ce (up to 173 ppm, mean = 41 ppm). Yttrium contents reach 67 ppm, with a mean value of 25 ppm. Post-Archean Australian Shale (PAAS)-normalized REY patterns (Fig. 9) show horizontal to slightly positive slopes ($[\mathrm{La/Sm}]_{\mathrm{PAAS-N}}$ = 0.3–1.5, mean = 0.6; $[\mathrm{Sm/Yb}]_{\mathrm{PAAS-N}}$ = 0.3–1.1, mean = 0.6) with absent to positive Ce anomalies ($[\mathrm{Ce/Ce^*}]_{\mathrm{PAAS-N}}$ = 0.9–5.5, mean = 1.4).

Correlation plots reveal strong positive relationships between SiO_2 and Al_2O_3 ($R^2 = 0.86$; Fig. 10A) and Na_2O ($R^2 = 0.80$; Fig. 10B), which agrees with the presence of aluminosilicate detrital particles (Fig. 8). SiO_2 also correlates with Rb ($R^2 = 0.52$), Zr ($R^2 = 0.36$), and Ge ($R^2 = 0.48$; Fig. 10C), but shows virtually no correlation with K_2O ($R^2 = 0.002$; Fig. 10D). MnO correlates with K_2O ($R^2 = 0.51$; Fig. 10E), suggesting K incorporation in Mn oxides. Poor correlation between BaO and MnO ($R^2 = 0.02$; Fig. 10F) indicates general absence of Ba-Mn oxides (e.g., hollandite). Cobalt shows moderate correlation with Mn ($R^2 = 0.31$; Fig. 10G) and other trace metals including Pb ($R^2 = 0.58$), Bi ($R^2 = 0.60$), Te ($R^2 = 0.31$), and In ($R^2 = 0.63$; Fig. 10H). REY are virtually uncorrelated with SiO_2 ($R^2 = 0.002$; Fig. 10C) or P_2O_5 ($R^2 = 0.012$), and weakly correlated with MnO ($R^2 = 0.135$), suggesting their primary occurrence in Mn oxides.

Major mineralogy

X-ray diffraction analysis of 47 manganese-oxide samples from the Chilcatay and Pisco formations indicates predominance of manganese oxides and silicate minerals including quartz, plagioclase, mica, and clays (Fig. 11). Additional detected phases include gypsum, anhydrite, and rare dolomite, which based on textural observations likely represent chemical precipitates. The identified manganese oxides include either cryptomelane or hollandite, and todorokite or buserite. Although these mineral pairs are indistinguishable by X-ray diffraction patterns (e.g., Burns and Burns 1977; Pelleter et al. 2017), the EPMA data presented below indicate that buserite is absent.

The results allow classification of the studied samples into two main mineralogical groups according to the dominant manganese oxide: (i) cryptomelane/hollandite type, and (ii) todorokite type (Fig. 11). All Mn oxide forming specks and incipient micronodules in mudstone (samples 2022-PAL- 14, 2022-PAL- 16/17, 2023-PAL- 09/10, and 2023-PAL- 44) consistently belong to the todorokite-type group, as well as two manganese coatings (samples 2022-PAL- 06 and 2023-PAL- 46). The remaining samples yielded similar XRD patterns consistent with cryptomelane/hollandite.

Mineral geochemistry

Both cryptomelane/hollandite and todorokite type samples were analyzed by EPMA. Table 2 summarizes the results, including minimum, maximum, geometric mean, and interquartile range values.

In cryptomelane/hollandite-type samples, Mn-oxide minerals mainly consist of MnO (49.0–79.5 wt%) and K_2O (1.11–6.62 wt%). Other elements occurring in high but erratic contents include FeO (< 13.2 wt%), SiO_2 (< 17.7 wt%), and Al_2O_3 (< 8.50 wt%). These irregular values may partly reflect mineral admixtures. Elements found in lesser proportions include Na_2O (< 2.57 wt%), P_2O_5 (< 2.50 wt%), TiO_2 (< 2.30 wt%), MgO (< 1.98 wt%), NiO (< 0.68 wt%), SO_3 (< 0.64 wt%), CaO (< 0.63 wt%), ZnO (< 0.39 wt%), PbO (< 0.25 wt%), and BaO (< 1.17 wt%). CoO contents range from below detection limit to 2.1 wt%, with a mean value of 0.38 wt%. The substantially higher K_2O than BaO values in most analyses indicate predominance of cryptomelane $[K(Mn^{4+},Mn^{3+})_8O_{16}]$ over hollandite $[Ba(Mn^{4+},Mn^{3+})_8O_{16}]$.

In todorokite-type samples, Mn-oxide materials primarily comprise MnO (45.8–65.5 wt%) and MgO (3.48–5.01 wt%). Minor elements include Al_2O_3 (< 3.90 wt%), CaO (<

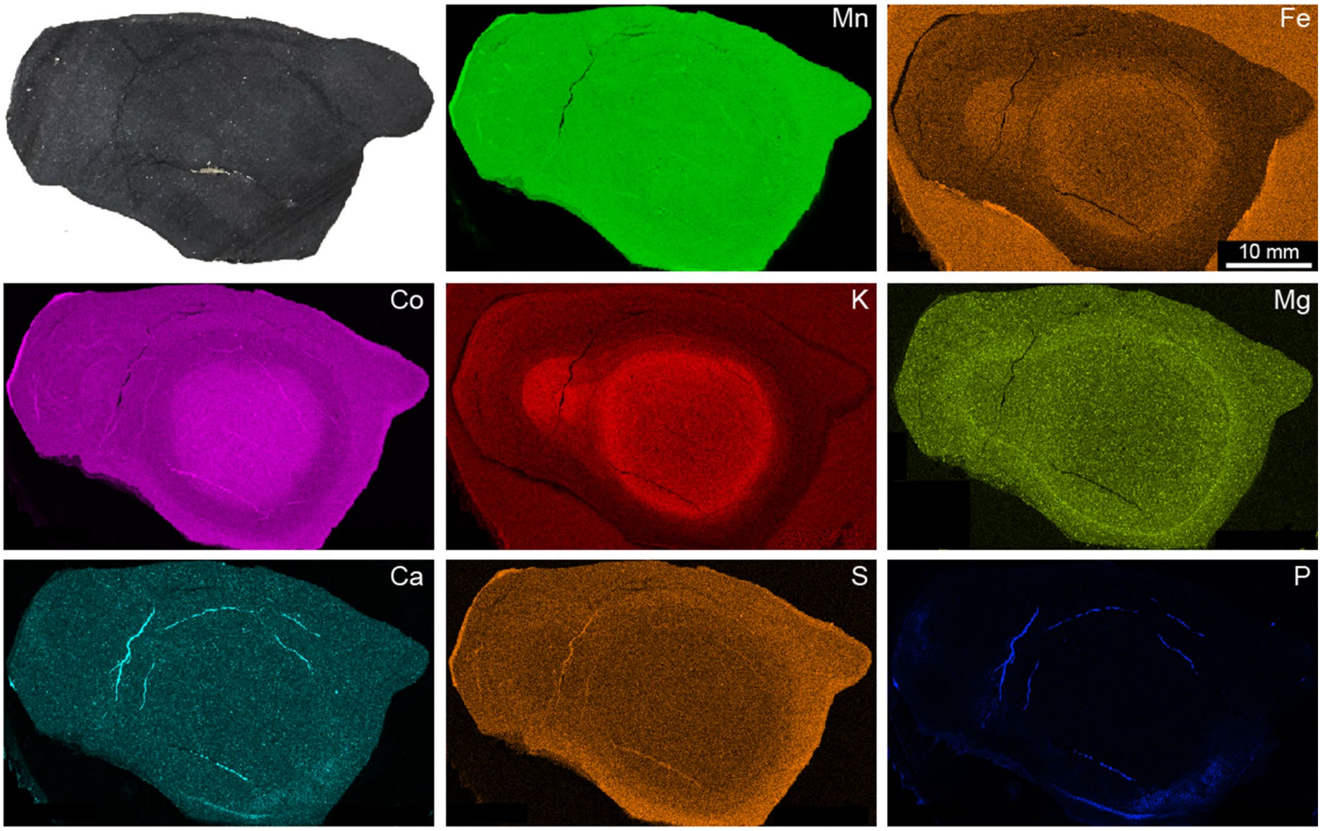

Fig. 6 Micro-XRF maps showing the distribution of selected elements in a massive Mn-oxide nodule from the East Pisco Basin [sample 2022-PAL- 04]

1.70 wt%), Na_2O (< 1.49 wt%), BaO (< 1.37 wt%), and K_2O (< 1.07 wt%). High SiO_2 values (< 19.6 wt%) in some analyses are attributed to mineral admixtures. Elements present in lesser amounts include P_2O_5 (< 0.27 wt%), TiO_2 (< 0.41 wt%), NiO (< 0.21 wt%), and FeO (< 1.88 wt%). CoO contents range from below detection limit to 2.6 wt%, with a mean value of 0.19 wt%.

Discussion

Origin of the Mn-oxide mineralization: stratigraphic, textural, and mineralogical evidence

The stratabound distribution of Mn-oxide nodules and concretions alongside Mn-oxide veins and coatings (Figs. 3 and 4) provide compelling evidence that Mn-rich fluids were mobilized through different sedimentary levels, ruling out a hydrogenetic origin (direct precipitation from seawater). The shallow water environment (Di Celma et al. 2016; Gioncada et al. 2018; Bosio et al. 2024) and high sedimentation rates (Gariboldi et al. 2017) in the East Pisco Basin are also inconsistent with environments typical for hydrogenetic Mn oxide precipitation (cf. Hein and Koschinsky 2014; Hein et al. 2020). Instead, the evidence strongly supports that the Mn-oxide veins resulted from focused circulation of Mn-rich fluids along fractures throughout the East Pisco Basin. The accumulation of Mn-oxide nodules along gypsum-Mn-oxide veins or around "chimney-like" structures (Fig. 4H) strongly suggests that veins and other structures associated with fluid circulation served as feeders for the formation of nodules and concretions in discharge zones in permeable sedimentary levels. In cases where permeable layers are "sealed" by overlying massive gypsum beds, Mn oxides may form "grape-like" composite concretions hanging from the gypsum base (Fig. 4E), further emphasizing the stratigraphic control on the mobilization and precipitation of Mn oxides. The fact that the Mn-oxide mineralization in nodules and concretions occurs as cement to (bio)clastic particles (Fig. 8A-F) within primary interparticle porosity further stresses its secondary origin relative to sedimentation (Chan 2022).

These observations raise two possible origins of the Mn oxide mineralization in the East Pisco Basin: diagenetic or hydrothermal. The nodular growth of Mn oxides is more characteristic of diagenetic processes rather than hydrothermal systems, with the former typically featuring slow, diffusion-controlled precipitation around nucleation sites under

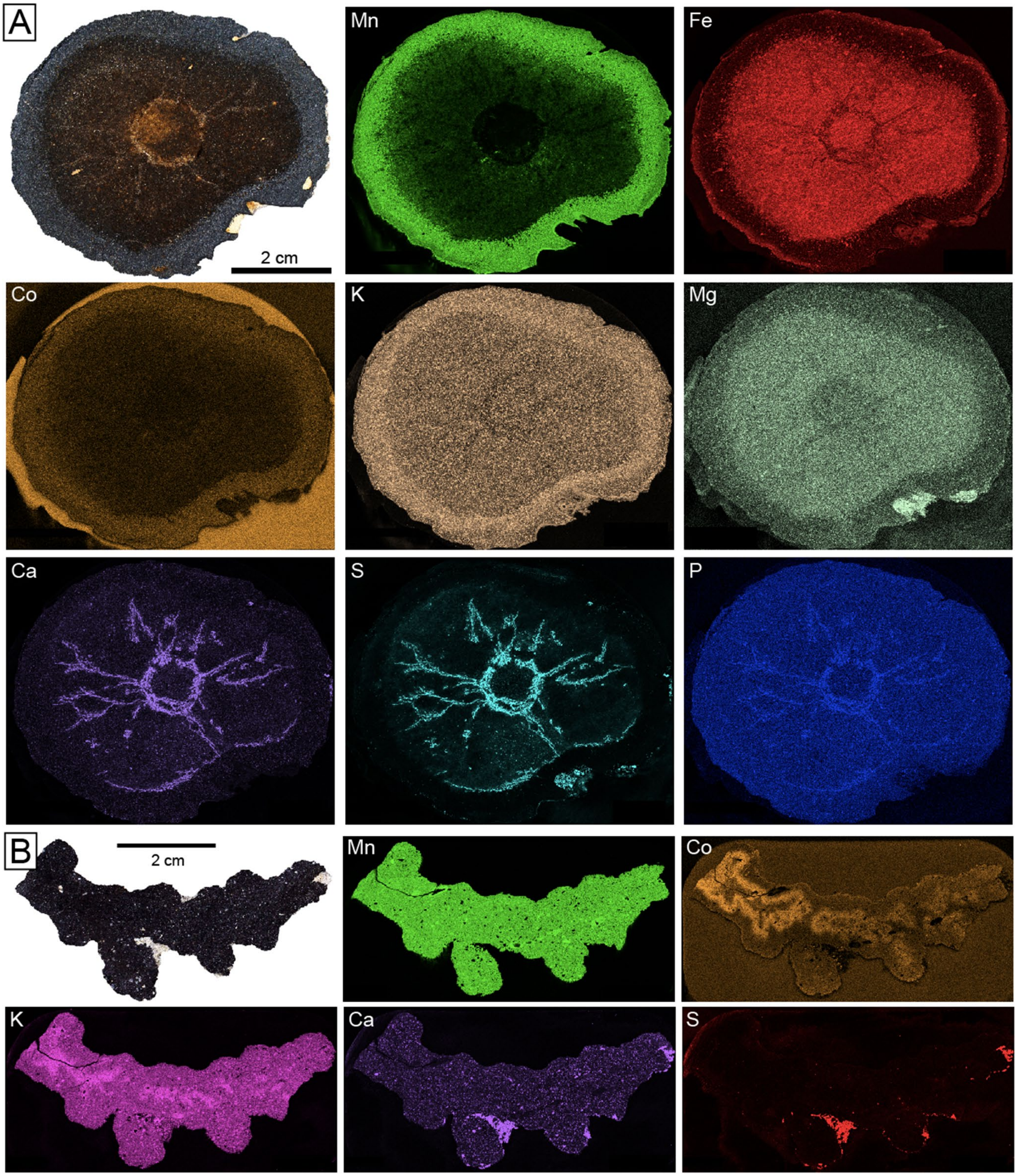

Fig. 7 Micro-XRF maps showing the distribution of selected elements in a complex nodule comprising a rind of Mn oxides around a claystone mantle and core [sample 2023-PAL- 48] (**A**) and a dendritic-botryoidal composite concretion [sample 2023-PAL- 29] (**B**) from the East Pisco Basin

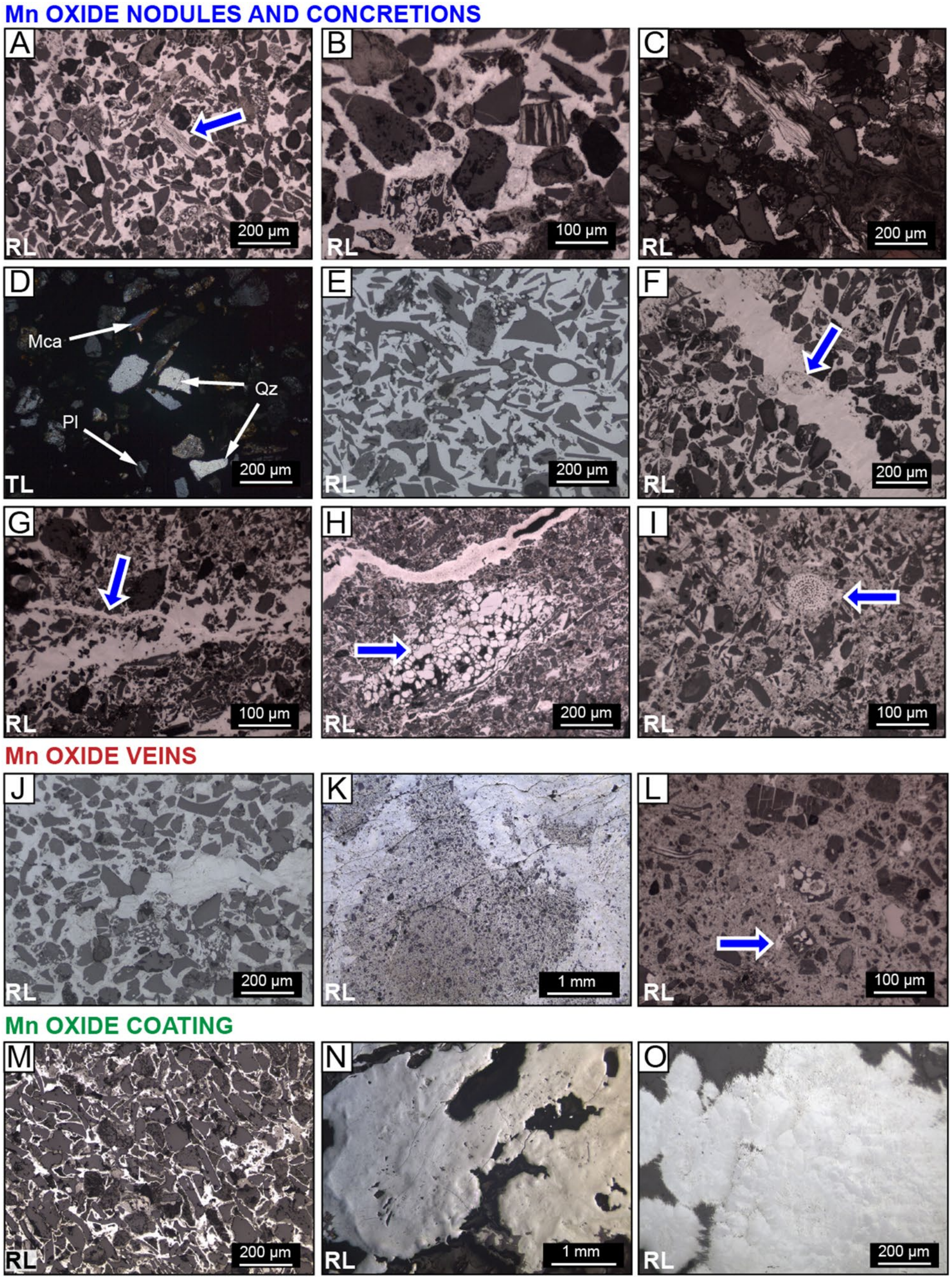

Fig. 8 Photomicrographs of representative microtextures in Mn-oxide nodules (**A**-**I**), veins (**J**-**L**), and coatings (**M**-**O**) from the Chilcatay and Pisco formations in the East Pisco Basin. **A** Manganese-oxide cement to detrital particles with low interparticle porosity. Fibrous remnant of probable vegetal origin (blue arrow) fossilized by Mn oxides [2023-PAL- 35]. **B** Close-up of Mn oxides cementing detrital particles in a cement-supported fabric [2023-PAL- 34]. **C** Minor Mn-oxide cement to detrital particles in sample with a high proportion of interparticle porosity [2023-PAL- 48B]. **D** Angular detrital particles of quartz, plagioclase, and mica cemented by Mn oxides [2023-PAL- 47]. **E** Juvenile glass shards cemented by Mn oxides in tuff [2023-PAL- 36]. **F** Thin (< 200 µm wide) massive Mn-oxide veinlet cutting across a mass of detrital grains cemented by Mn-oxide cement; several sub-rounded clasts containing Mn-oxides with detrital material are incorporated within the massive vein (blue arrow) [2023-PAL- 34]. **G** Porous and thin Mn-oxide veinlet (blue arrow) crosscuts a more massive and thicker Mn-oxide vein [2023-PAL- 43]. **H** Porous, colloidal Mn-oxide vein infill; possible siliceous remnants of diatoms are also observed (blue arrow) [2022-PAL- 04]. **I** Framboidal organic structure fossilized by Mn oxides (blue arrow); Mn oxides also occur as a cement of detrital particles [2022-PAL- 10]. **J** Massive Mn-oxide cement to detrital particles with only very local interparticle microporosity [2023-PAL- 38]. **K** Alternating domains of massive Mn oxides and zones with higher proportions of detrital grains and porosity [2022-PAL- 03]. **L** Square organic structure fossilized by Mn oxides (blue arrow); Mn oxides also occur as a cement of other detrital particles [2022-PAL- 03]. **M** Minor Mn-oxide cement to detrital particles in sample with a high proportion of interparticle porosity [2023-PAL- 02]. **N** Massive, gel-like colloidal Mn oxides with only local microporosity [2023-PAL- 19]. **O** Massive Mn-oxide mineralization with internal botryoidal, gel-like texture and micro-urchin terminations [2023-PAL- 19]. Abbreviations: Mca—Mica; Pl—Plagioclase; Qz—Quartz; RL—Reflected light; TL—Transmitted light

Table 1 Bulk contents of selected elements in Mn oxides from the East Pisco Basin, sorted by morphological type. Presented data include minimum (MIN), maximum (MAX), geometric mean (GM), and inter-quartile range (IQR) values, all expressed in wt%

		All data ($n = 23$)				Nodule/concretion ($n = 14$)				Vein ($n = 3$)				Coating ($n = 5$)				Bioturbation replacement
Analyte	Units	MIN	MAX	GM	IQR	MIN	MAX	GM	IQR	MIN	MAX	GM	IQR	MIN	MAX	GM	IQR	(1 analysis)
SiO_2 (XRF)	%	10.54	56.45	24.18	30.36 - 19.77	16.28	56.45	25.20	30.34 - 19.88	14.68	29.77	20.63	24.93 - 17.38	10.54	34.72	23.12	30.95 - 24.12	27.37
Al_2O_3 (XRF)	%	1.31	12.94	5.85	7.27 - 5.19	4.25	12.94	6.52	7.64 - 5.48	3.95	7.40	5.27	6.21 - 4.49	1.31	7.95	4.43	6.66 - 4.89	7.02
CaO (XRF)	%	0.53	13.30	1.68	2.32 - 0.90	0.69	13.30	1.45	2.08 - 0.88	0.53	1.29	0.80	1.03 - 0.65	1.04	13.23	4.15	7.58 - 1.68	1.27
BaO (XRF)	%	0.03	0.99	0.15	0.26–0.90	0.03	0.99	0.20	0.30 - 0.12	0.04	0.24	0.09	0.16 - 0.06	0.03	0.33	0.10	0.16 - 0.05	0.20
Na_2O (XRF)	%	1.10	3.21	1.99	2.34 - 1.75	1.41	3.21	2.04	2.22 - 1.77	1.42	2.49	1.83	2.12 - 1.58	1.10	2.45	1.92	2.44 - 1.98	2.21
K_2O (XRF)	%	0.44	4.13	2.66	3.37 - 2.64	0.92	4.13	2.96	3.58 - 2.80	2.75	3.52	3.20	3.46 - 3.07	0.44	3.14	1.73	2.77 - 1.93	2.79
TiO_2 (XRF)	%	0.07	0.50	0.21	0.24 - 0.20	0.10	0.50	0.24	0.24 - 0.21	0.13	0.28	0.20	0.25 - 0.17	0.07	0.23	0.15	0.19 - 0.17	0.31
Fe_2O_3 (XRF)	%	0.90	9.73	2.33	3.02 - 1.47	0.90	8.68	2.17	2.44 - 1.33	1.54	3.51	2.37	2.99 - 2.01	1.39	4.45	2.13	2.53 - 1.52	9.73
MgO (XRF)	%	0.71	15.47	1.30	1.39 - 0.87	0.82	10.68	1.25	1.36 - 0.88	0.71	0.88	0.81	0.87 - 0.79	0.93	15.47	2.08	1.72 - 1.03	0.95
MnO (XRF)	%	4.85	55.69	34.71	47.21 - 31.50	4.85	52.23	34.16	47.36 - 35.51	37.84	55.69	46.85	52.24 - 43.32	20.33	45.72	30.39	43.38 - 25.01	34.31
P_2O_5 (XRF)	%	0.16	1.19	0.61	0.85 - 0.51	0.16	0.95	0.54	0.82 - 0.48	0.61	0.88	0.77	0.87 - 0.74	0.38	1.19	0.69	0.82 - 0.59	0.76
SO_3 (XRF)	%	0.10	9.62	0.52	1.13 - 0.23	0.10	1.57	0.43	0.92 - 0.26	0.15	0.24	0.20	0.23 - 0.18	0.36	9.62	1.96	7.18 - 0.92	0.16
C (LECO)	%	0.02	5.29	0.07	0.06 - 0.03	0.03	4.92	0.07	0.10 - 0.03	0.04	0.06	0.05	0.06 - 0.05	0.02	5.29	0.09	0.06 - 0.02	0.05
S (LECO)	%	0.04	3.75	0.19	0.41 - 0.09	0.04	0.59	0.17	0.34 - 0.10	0.05	0.09	0.07	0.08 - 0.06	0.13	3.75	0.72	2.86 - 0.31	0.06
V (ICP-MS)	ppm	32	736	180	376 - 105	39	736	201	376 - 126	32	522	97	289 - 44	99	280	156	199 - 117	449
Co (ICP-AES)	ppm	111	6290	1650	2895 - 1240	111	6290	1575	3198 - 1193	1830	4230	2469	3088 - 1888	428	2960	1492	2550 - 1115	1555
Ni (ICP-AES)	ppm	40	1405	140	210 - 69	40	1405	110	147 - 56	88	147	105	119 - 89	127	833	344	516 - 198	119
Cu (ICP-AES)	ppm	16	496	137	237 - 101	35	496	179	357 - 144	124	324	208	275 - 175	16	111	45	99 - 18	227
Zn (ICP-AES)	ppm	111	1330	323	434 - 224	111	810	268	362 - 217	209	356	292	345 - 272	342	1330	560	530 - 442	383
As (ICP-MS)	ppm	16	> 250	142	250 - 105	16	> 250	151	250 - 118	83	243	136	184 - 104	47	> 250	104	172 - 62	236
Y (ICP-MS)	ppm	7	67	25	37 - 16	7	67	21	28 - 15	33	59	40	46 - 33	12	50	24	41 - 15	59
Mo (ICP-AES)	ppm	<d.l.	432	39	201 - 21	<d.l.	432	64	225 - 29	<d.l.	20	3	11 - 1	4	198	47	165 - 26	44
Cd (ICP-AES)	ppm	6	> 1000	120	273 - 43	6	925	85	253 - 31	17	273	93	224 - 95	170	> 1000	322	378 - 199	241
Sb (ICP-MS)	ppm	0.6	27.0	3.4	7.8 - 1.3	0.9	27.2	5.1	9.2 - 2.4	1.0	2.6	1.4	1.9 - 1.1	0.6	5.9	1.9	3.5 - 1.1	2.5
Tl (ICP-MS)	ppm	0.82	> 250	44.04	80.40 - 41.90	0.82	> 250	34.26	80.40 - 17.85	17.05	128.50	48.57	90.40 - 34.68	48.80	> 250	82.69	109.30 - 58.25	69.20
Pb (ICP-AES)	ppm	15	784	69	73 - 47	15	784	78	89 - 52	66	269	108	170 - 68	23	59	40	49 - 37	55
REE (ICP-MS)	ppm	15	238	93	132 - 75	45	238	99	132 - 75	75	173	116	147 - 97	15	111	56	97 - 52	142
REY (ICP-MS)	ppm	27	268	121	188 - 92	52	268	122	181 - 92	108	207	159	193 - 144	27	160	82	138 - 67	201

For the calculation of geometric mean (GM) and interquartile range (IQR) values, measurements below or above detection limits were substituted with their respective detection limit values

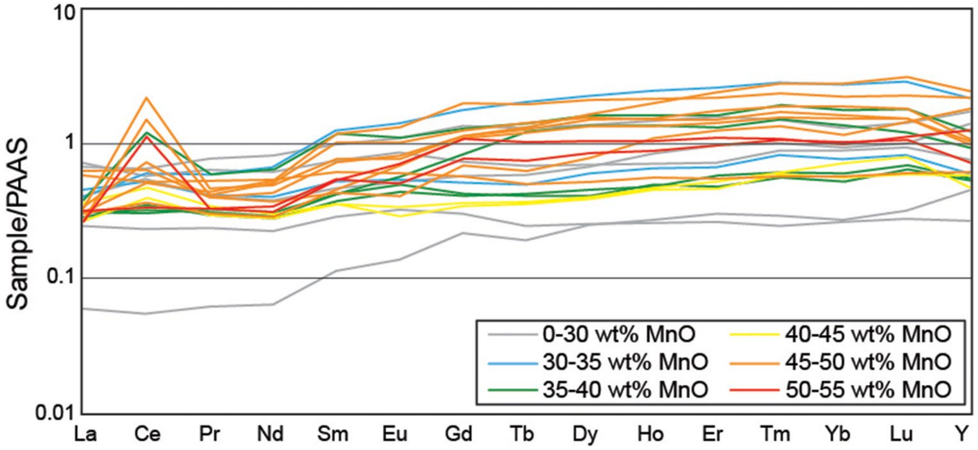

Fig. 9 PAAS-normalized REY patterns of the Mn oxides from the East Pisco Basin (PAAS values after McLennan 1989)

low-temperature conditions (Calvert and Price 1977; Jiang et al. 2019). In contrast, hydrothermal manganese mineralization tends to form dominantly stratiform, crustiform, or vein-type deposits due to rapid precipitation rates and higher-energy conditions (Hein et al. 2000; Hein and Koschinsky 2014). The fossilization of bioturbation (Fig. 5M, N) and organic structures (e.g., diatoms; Fig. 8A, H-I, L) by Mn oxides is also typical for mineralization of diagenetic origin (Achurra et al. 2009; Chan 2022). Cryptomelane, the major Mn mineral identified in Mn-oxide nodules, veins, and coatings (Fig. 11), can be of diagenetic origin (Vodyanitskii et al. 2004) and has been identified in onshore diagenetic nodules from the Bahía Inglesa Formation in Chile (Achurra et al. 2009). Todorokite, which is restricted to Mn micronodules and two Mn coatings in the studied samples, is also consistent with a diagenetic origin of the Mn-oxide mineralization, although it is also common in hydrothermal Mn oxide deposits (Hein and Koschinsky 2014).

Several processes have been proposed to explain the genesis of diagenetic Mn oxides in general and of Mn nodules and concretions in particular. These models generally describe reductive dissolution of Mn and other metals (e.g., Ni, Cu, Zn) in the upper part of the sediment column during organic matter decomposition in early diagenesis (Koschinsky et al. 2010). In this process, dissolved Mn accumulates in the porewater and subsequently reprecipitates when exposed to oxidizing conditions. However, this relatively simple diagenetic model cannot adequately explain the extensive vertical distribution of Mn-oxide mineralization observed in the East Pisco Basin (spanning 185 m in stratigraphic column C2; Fig. 3), nor does it account for the compelling evidence of structure-focused fluid flow throughout the basin.

In Jurassic sandstone from Utah, Chan et al. (2000) describe the occurrence of Fe and Mn oxides, including hematite, pyrolusite, manganite, and cryptomelane-hollandite, either cementing quartz sand grains in concretions and stratiform bodies or filling fractures that parallel a major structure, the Moab Fault. Chan et al. (2000) propose that faulting and salt tectonism caused the dissolution of a salt-cored anticline through interaction with meteoric water. The resulting saline brines were reduced by reaction with hydrocarbons, organic acids, or hydrogen sulfide. This saline, reduced fluid flowed upward through the Moab Fault and adjacent permeable red sandstone, leaching Fe and Mn. Upon entering the regional aquifer system, the metal-charged fluid mixed with shallow, oxygenated groundwater, triggering precipitation of Fe and Mn oxides within porous and permeable sandstone beds.

In the East Pisco Basin, Gioncada et al. (2018) documented scarce Fe and Mn oxides associated with diagenetic dolomite in and around fossils in the Pisco Formation. These authors propose that organic matter decay within shallow-marine, organic-rich sediments, coupled with Mn and Fe reduction, enriched these elements in sediment porewater. Porewater sulfate, acting as an oxidizing agent for organic matter, led to Fe sulfide formation, evidenced by abundant ghost framboidal pyrite. The high-Mn/Fe oxides subsequently precipitated either due to increased alkalinity resulting from sulfate reduction or from renewed interaction with oxygenated seawater at the seafloor following organic matter depletion. In this context, onshore Mn oxides from the Chilcatay and Pisco formations could be related to the decomposition of organic matter at the bottom of the shallow marine East Pisco basin, as described by Gioncada et al. (2018). As an alternative to this local-scale process, regional-scale hydrocarbon migration could have also played a significant role. Hydrocarbon seepage (Rossello et al. 2022) and gas chimneys (Calvès et al. 2017) are common features in the Peruvian forearc basins, for which a high hydrocarbon potential has long been recognized, including the Pisco Basin (Travis et al. 1976; Crouch et al. 1990). The oily black stains observed in East Pisco Basin rocks provide direct evidence of liquid hydrocarbon circulation within the study area. In this line of evidence, saline fluids derived from local evaporitic basins that formed during the sedimentation of the Pisco Formation (Gioncada et al. 2018) could have become chemically reduced through interaction with these hydrocarbons, similar to the process proposed by Chan et al. (2020) for Mn oxides in the Jurassic sandstone in Utah. Noteworthy, hydrocarbon-related ferromanganese nodules have been documented in a few offshore continental margins affected by hydrocarbon-rich fluid venting seepage, but in general they have received relatively little scientific attention (see González et al. 2009, 2012).

We propose that reduced fluids, whether generated by in situ organic matter decay or through interaction with hydrocarbons, migrated through structural pathways and permeable beds throughout the East Pisco Basin. The fluid migration pathways were influenced by stratigraphic architecture, with some permeable beds being "sealed" by overlying massive gypsum layers that acted as stratigraphic traps, focusing fluid flow laterally. The basin-wide distribution of Mn oxides—from siltstones of the Chilcatay Formation to the upper part of the Pisco Formation (considered Pliocene in age; Ochoa et al. 2021)—indicates that Mn-oxide precipitation must be Pliocene or younger. We suggest that the rapid uplift of the East Pisco Basin during the late Pliocene, triggered by the oblique subduction of the aseismic Nazca Ridge beneath the South American Plate beginning ca. 4–5 Ma (Macharé and Ortlieb 1992; Hampel 2002; Espurt et al. 2007; George et al. 2022), likely promoted fluid mobilization through mechanisms such as decompression or seismic pumping (cf. Hunt 1996; Eisenlohr et al. 1994). The precipitation of Mn oxides occurred when these reduced, Mn-rich fluids subsequently mixed with oxidizing fluids, either shallow oxygenated seawater (Gioncada et al. 2018) or groundwater (Chan et al. 2000), completing the geochemical cycle necessary for Mn-oxide formation throughout the stratigraphic sequence.

Origin of the Mn-oxide mineralization: geochemical discrimination diagrams

Different geochemical genetic discrimination plots for Mn-oxide mineralization have been proposed in the literature (e.g., Bonatti et al. 1972; Josso et al. 2017; Zawadzki et al. 2022). Bulk and EPMA results from this study are plotted in some of such diagrams, along with previous analyses of Mn-oxide nodules from another site within the Pisco Formation by Bessler (1975) for comparison (Fig. 12). In the Fe-Mn-(Cu + Co + Ni) × 10 diagram, the data plot in the overlapping area of the hydrothermal and early diagenetic fields (Fig. 12A). Likewise, in the (Fe + Mn)/4 - (Ni + Cu) × 15 - (Zr + Y + Ce) × 100 diagram, the data plot in the area of hydrothermal and suboxic diagenetic origins (Fig. 12B). Therefore, the representation of our data in both diagrams concurs with the proposed diagenetic origin of the Mn oxides in the East Pisco Basin, but is inconclusive as to whether there was hydrothermal imprint.

In the Ce/Ce* vs. $(Y/Ho)_{PAAS-N}$ diagram, most samples fall between the hydrogenetic and hydrothermal fields, with a remarkable dispersion (Fig. 12C). Therefore, this plot does not provide clear conclusions regarding the origin of the Mn mineralization. Although hydrogenetic nodules characteristically exhibit positive Ce anomalies, Ce can migrate simultaneously to Mn and later be incorporated into Mn oxides during the reoxidation and precipitation of Mn at oxic-anoxic interfaces (Zhang et al. 2023).

Metalliferous interest and exploration guidelines

In addition to high manganese (mean = 34.7 ± 12.4 wt% Mn), the Mn oxide nodules, veins, and crusts from the East Pisco Basin yield significant cobalt contents, which are up to 0.63 wt% Co (mean = 0.16 ± 0.15 wt% Co) in bulk analyses, and up to 2.08 wt% Co (mean = 0.36 ± 0.33 wt% Co) in EPMA data (Tables 1 and 2). These values are comparable to those in hydrogenetic Mn-oxide mineralization from the Cook Islands-Penrhyn Basin (mean = 0.38 wt% Co) and in mixed (hydrogenetic-hydrothermal)-type Mn-oxide nodules from the Clarion Clipperton Zone and other abyssal plains (mean = 0.24 wt% Co; Hein et al. 1997; Hein and Koschinsky 2014). In contrast, cobalt values in Mn oxides from the East Pisco Basin are higher than those in mixed-type Mn nodule deposits in the Central Indian Ocean Basin (mean = 0.11 wt% Co), and in diagenetic Mn nodules from the Peru Basin (mean = 0.05 wt% Co) according to data compiled by Hein et al. (2020). Noteworthy, this finding contrasts with the typically low Co contents of diagenetic nodules in general (< 0.1 wt%; Hein and Koschinsky 2014).

The reason for the exceptional Co enrichment in the Mn-oxide mineralization of the East Pisco Basin remains enigmatic, particularly when compared to Mn-oxide nodules from the nearby Bahía Inglesa Formation in Chile (< 0.05 wt% Co; Achurra et al. 2009). This comparison is especially intriguing given the numerous similarities between these deposits: (i) diagenetic Mn oxides including nodules, (ii) Miocene marine sedimentary host rocks deposited in restricted environments, and (iii) abundant gypsum/anhydrite veins crosscutting the sequence. The marked contrast in Co contents may reflect differences in depositional settings, including coastal upwelling (Böning et al. 2004) or distance of deposition of continental-shelf seafloor sediments from river-dominated continental margins (Lenstra et al. 2022). Both mechanisms can potentially contribute trace metals and promote organic matter production through nutrient availability. It is worth to note that the Pisco Formation accumulated within an upwelling-dominated ecosystem, likely representing an early manifestation of what

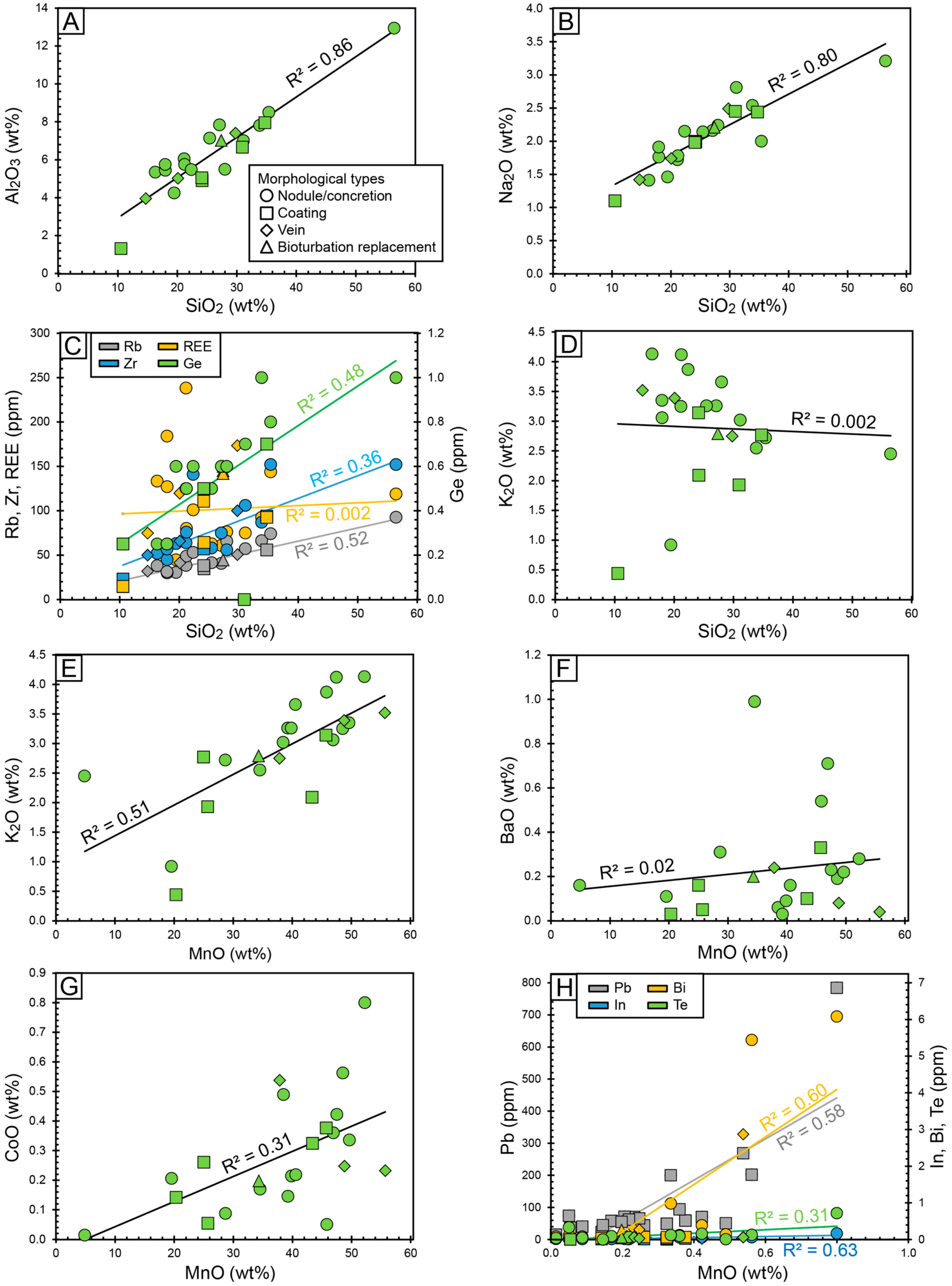
A
R² = 0.86
Al2O3 (wt%)
SiO2 (wt%)
Morphological types
○ Nodule/concretion
□ Coating
◇ Vein
△ Bioturbation replacement
B
R² = 0.80
Na2O (wt%)
SiO2 (wt%)
C
Rb
Zr
REE
Ge
R² = 0.48
R² = 0.36
R² = 0.002
R² = 0.52
Rb, Zr, REE (ppm)
Ge (ppm)
SiO2 (wt%)
D
R² = 0.002
K2O (wt%)
SiO2 (wt%)
E
R² = 0.51
K2O (wt%)
MnO (wt%)
F
R² = 0.02
BaO (wt%)
MnO (wt%)
G
R² = 0.31
CoO (wt%)
MnO (wt%)
H
Pb
Bi
In
Te
R² = 0.60
R² = 0.58
R² = 0.31
R² = 0.63
Pb (ppm)
In, Bi, Te (ppm)
MnO (wt%)

Fig. 10 Binary correlation plots for selected elements in bulk samples of Mn-oxide nodules, veins, and coatings. **A** SiO_2 vs. Al_2O_3 (wt%). **B** SiO_2 vs. Na_2O (wt%). **C** SiO_2 (wt%) vs. Rb, Zr, REE (ppm) in main axis, and SiO_2 (wt%) vs. Ge (ppm) in secondary axis. **D** SiO_2 vs. K_2O (wt%). **E** MnO vs. K_2O (wt%). **F** MnO vs. BaO (wt%). **G** CoO vs. BaO (wt%). **H** CoO (wt%) vs. Pb (ppm) in main axis, and CoO (wt%) vs. In, Bi, Te (ppm) in secondary axis

would evolve into the modern Humboldt current system (Collareta et al. 2021; Bosio et al. 2024).

An additional or alternative possibility is that differentially deeper fluid circulation throughout the sedimentary pile and basement rocks may have contributed to the Co endowment. A conspicuous geographic feature of the study area is its location above the subducting Nazca Ridge and at the same latitude as the Nazca Drift System (Figs. 1 and 2A). Calvès et al. (2022) suggest that the large volumes of accumulated sediments and polymetallic material, as well as excess pore water in the Nazca Drift System, may have influenced Andean orogenesis and metallogenesis since the middle-late Miocene. Subduction-derived water circulating in the forearc domain may have scavenged Co from underlying basement rocks, particularly those of mafic composition in the Coastal Basal Complex beneath the Cenozoic sedimentary sequence of the East Pisco Basin (Ochoa et al. 2021). The irregular Co enrichment observed in nodules (Figs. 6 and 7) supports the interpretation that Co-rich fluid supply was pulsatile, likely involving fluctuating proportions of fluids from different sources or evolutionary pathways.

It is important to note that the same scenarios proposed for differential Co enrichment in East Pisco Basin Mn oxides could equally explain the enrichment in other trace metals such as Cd, which reaches anomalously high contents in our samples (120 ± 280 ppm, with some values exceeding 1,000 ppm) compared to typical marine Mn nodules (1–10 ppm; Hein et al. 2013). Further investigation is necessary to elucidate the precise origin of the metals and the nature of the associated mineralizing fluids.

Although Mn oxides in the East Pisco Basin are irregularly distributed along different stratigraphic levels of the Chilcatay and Pisco formations (Figs. 3 and 4), Mn-bearing beds are laterally continuous, such that in some cases they could be followed for more than 300 m along strike. In addition, the accumulation of Mn-oxide nodule fragments in the stone pavement is so extensive that it imparts a dark color to the valley bottoms (Fig. 4A, B). These observations suggest an attractive volume of Mn-oxide mineralization in the study area. However, reliable grade and tonnage estimates cannot be established at this stage due to insufficient systematic grid sampling, limited documentation of full lateral extent, and a sampling approach that targeted Mn oxides specifically rather than collecting standardized, fixed-weight samples representing both mineralized material and host rock in their natural proportions.

Notwithstanding these uncertainties, our observations indicate that diagenetic Mn nodules from the East Pisco Basin represent a novel, previously overlooked cobalt mineralization style, suggesting that diagenetic Mn oxides may constitute prospective targets for this critical metal. These onshore Co-rich Mn oxide deposits offer an attractive alternative to controversial deep-sea mining operations. Key factors in the genesis of these Mn-oxide deposits—including high interstitial porosity in juvenile, poorly consolidated sediments that facilitated Mn-rich fluid circulation and oxide precipitation as cement—can guide identification of prospective stratigraphic horizons. Early-stage exploration strategies should also prioritize the identification of fluid-migration pathways (fractures and chimneys) that enabled Mn-rich fluids to enter extensive dynamic flow systems. Finally, since Mn nodules typically form extensive horizontal fields, satellite imagery can effectively identify prospective locations through their distinctive darker coloration relative to surrounding terrain, with eroded zones particularly favorable for accumulating nodule fragments as stone pavement.

Conclusions

The present study documents the morphological, mineralogical, and compositional variations of Mn oxides in the Chilcatay and Pisco formations exposed in the onshore forearc Pisco Basin in Peru. The main conclusions are the following:

- Manganese oxides occur as nodules and concretions, veins, and surface coatings that concentrate along particular sandstone, siltstone, and tuff levels. The lithological and stratigraphic control of the mineralization, the evidence of focused circulation of Mn-bearing fluids through fractures and chimney-like structures, the occurrence of Mn oxides cementing (bio)clastic particles, the fossilization of organic components by Mn oxides, and the crystallization as cryptomelane/hollandite and todorokite support a diagenetic origin of Mn-oxide mineralization.
- The Mn-oxide mineralization likely originated from either organic matter decomposition at the base of the shallow marine Pisco Basin or from interactions between brines and hydrocarbons, both processes promoting reductive dissolution of Mn and associated metals. Subsequently, the reduced, Mn-rich porewater migrated upward through fractures and discharged laterally along permeable horizons, particularly where impermeable

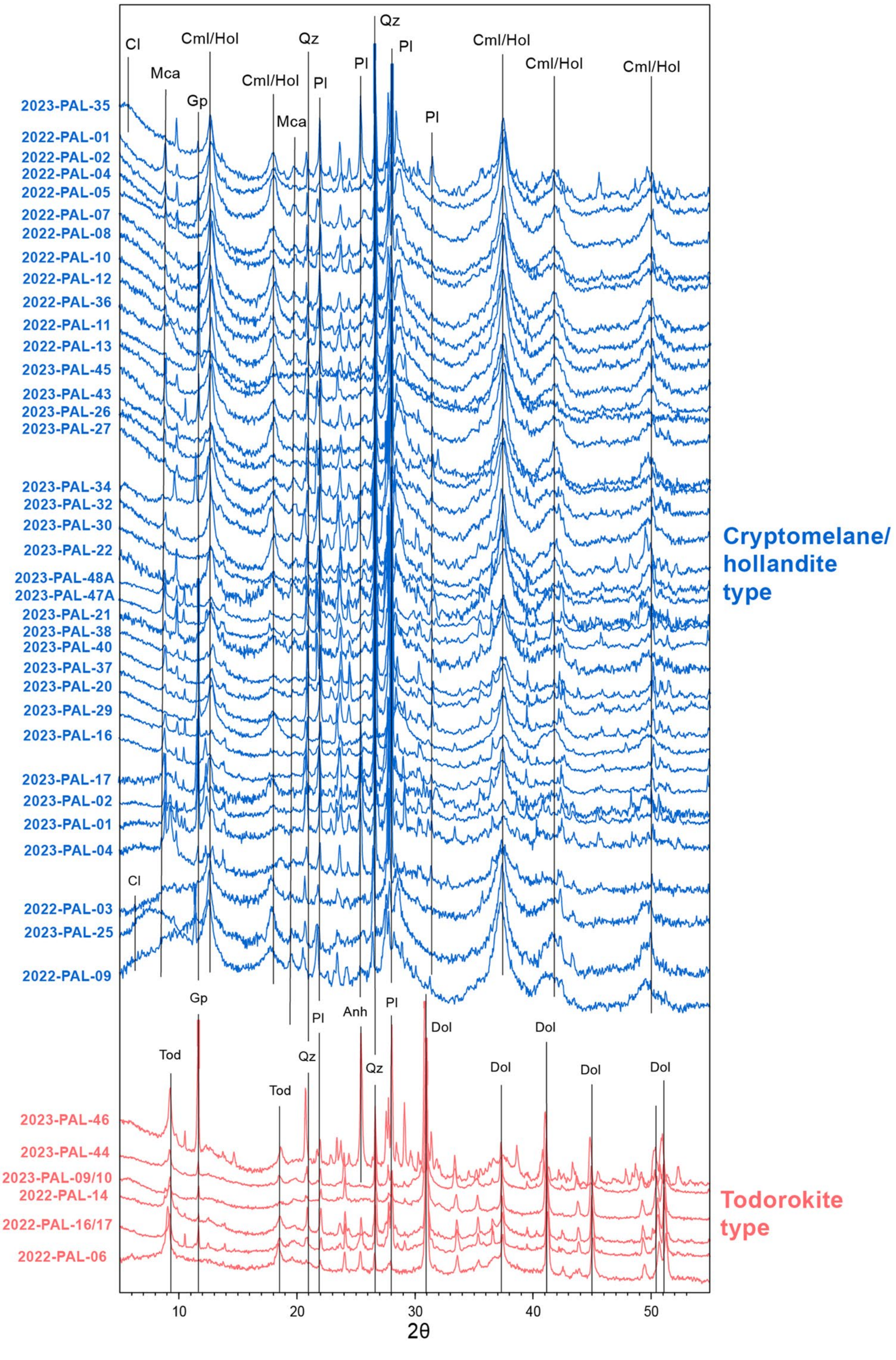

Fig. 11 XRD patterns divided into mineralogical categories according to the dominant Mn oxide. Major peaks are shown as black vertical lines with the corresponding mineral labels. Peaks at 2θ ~ 9.75° and ~ 10.50°, present in some samples, could not be correlated with any particular mineral phase. Abbreviations: Anh—Anhydrite; Cl—Clay; Cml/Hol—Cryptomelane/Hollandite; Dol—Dolomite; Gp—Gypsum; Mca—Mica; Pl—Plagioclase; Qz—Quartz; Tod—Todorokite

massive gypsum layers created effective hydrological and redox seals. The rapid uplift of the East Pisco Basin during the late Pliocene—driven by oblique subduction of the aseismic Nazca Ridge—may have enhanced fluid circulation through decompression dewatering or seismic pumping mechanisms while simultaneously establishing renewed oxygenated conditions that triggered precipitation of Mn oxides.

- Efficient Mn-oxide mineralization of diagenetic origin was enhanced by high interstitial porosity and sub-vertical structures connecting different stratigraphic levels and enabling the circulation of Mn-rich fluids within an extensive and dynamic flow system.
- The diagenetic manganese oxides from the East Pisco Basin have up to 0.63 wt% Co and a mean value of 0.17 wt% Co, which compares favorably with some

Table 2 Summary of the EPMA results on Mn oxides, including minimum (MIN), maximum (MAX), geometric mean (GM), and inter-quartile range (IQR) values expressed in wt%. Abbreviation:

	All analyses				Cryptomelane/hollandite type				Todorokite type			
	MIN	MAX	GM	IQR	MIN	MAX	GM	IQR	MIN	MAX	GM	IQR
SiO_2	<d.l.	19.6	0.32	0.6 - 0.1	<d.l.	17.7	0.30	0.5 - 0.1	<d.l.	19.6	1.8	11.3 - 0.3
Al_2O_3	<d.l.	8.5	0.43	0.9 - 0.2	<d.l.	8.5	0.42	0.9 - 0.2	<d.l.	3.9	0.73	3.3 - 0.1
CaO	<d.l.	1.7	0.18	0.2 - 0.1	<d.l.	1.3	0.16	0.2 - 0.1	1.2	1.7	1.4	1.5 - 1.3
K_2O	0.81	6.6	3.0	4.7 - 2.3	1.1	6.6	3.2	4.7 - 2.3	0.81	1.1	0.9	1.0 - 0.8
PbO	*<d.l.*	*0.25*	*0.16*	*0.2 - 0.2*	*<d.l.*	*0.25*	*0.16*	*0.2 - 0.2*	*<d.l.*	*<d.l.*	-	-
SO_3	*<d.l.*	*1.5*	*0.25*	*0.3 - 0.2*	*<d.l.*	*1.5*	*0.25*	*0.3 - 0.2*	*<d.l.*	*<d.l.*	-	-
P_2O_5	<d.l.	2.5	0.83	1.2 - 0.6	<d.l.	2.5	0.85	1.2 - 0.6	*<d.l.*	*<d.l.*	-	-
MgO	<d.l.	5.0	0.65	1.2 - 0.4	<d.l.	2.0	0.60	1.1 - 0.4	3.5	5.0	4.2	4.5 - 3.9
Na_2O	0.23	2.6	1.2	1.9 - 0.9	0.23	2.6	1.2	1.9 - 0.8	0.78	1.5	1.2	1.4 - 1.0
MnO	45.8	79.5	69.0	72.6 - 67.6	49.0	79.5	69.5	72.8 - 68.5	45.8	65.5	58.0	64.1 - 53.0
FeO	<d.l.	13.2	0.27	0.5 - 0.1	<d.l.	13.2	0.26	0.4 - 0.1	0.14	1.9	0.54	1.4 - 0.2
CoO	<d.l.	2.6	0.37	0.7 - 0.2	<d.l.	2.1	0.38	0.8 - 0.2	<d.l.	2.6	0.19	0.2 - 0.1
ZnO	*<d.l.*	*0.39*	*0.17*	*0.2 - 0.2*	*<d.l.*	*0.39*	*0.17*	*0.2 - 0.2*	<d.l.	0.25	0.19	0.2 - 0.2
CuO	*<d.l.*	*0.17*	*0.12*	*0.1 - 0.1*	*<d.l.*	*0.17*	*0.12*	*0.1 - 0.1*	*<d.l.*	*<d.l.*	-	-
NiO	*<d.l.*	*0.68*	*0.10*	*0.1 - 0.1*	*<d.l.*	*0.68*	*0.09*	*0.1 - 0.1*	<d.l.	0.21	0.14	0.2 - 0.1
TiO_2	*<d.l.*	*2.3*	*0.15*	*0.1 - 0.1*	*<d.l.*	*2.3*	*0.15*	*0.1 - 0.1*	*<d.l.*	*0.41*	*0.16*	*0.1 - 0.1*
BaO	*<d.l.*	*1.4*	*0.25*	*0.4 - 0.2*	*<d.l.*	*1.2*	*0.24*	*0.3 - 0.2*	0.34	1.4	0.67	0.9 - 0.4

For the calculation of geometric mean (GM) and interquartile range (IQR) values, measurements below detection limit (<d.l.) were substituted with their respective detection limit values

For datasets in which more than 50% of analyses fell below the detection limit, results are presented in italics to indicate reduced statistical reliability

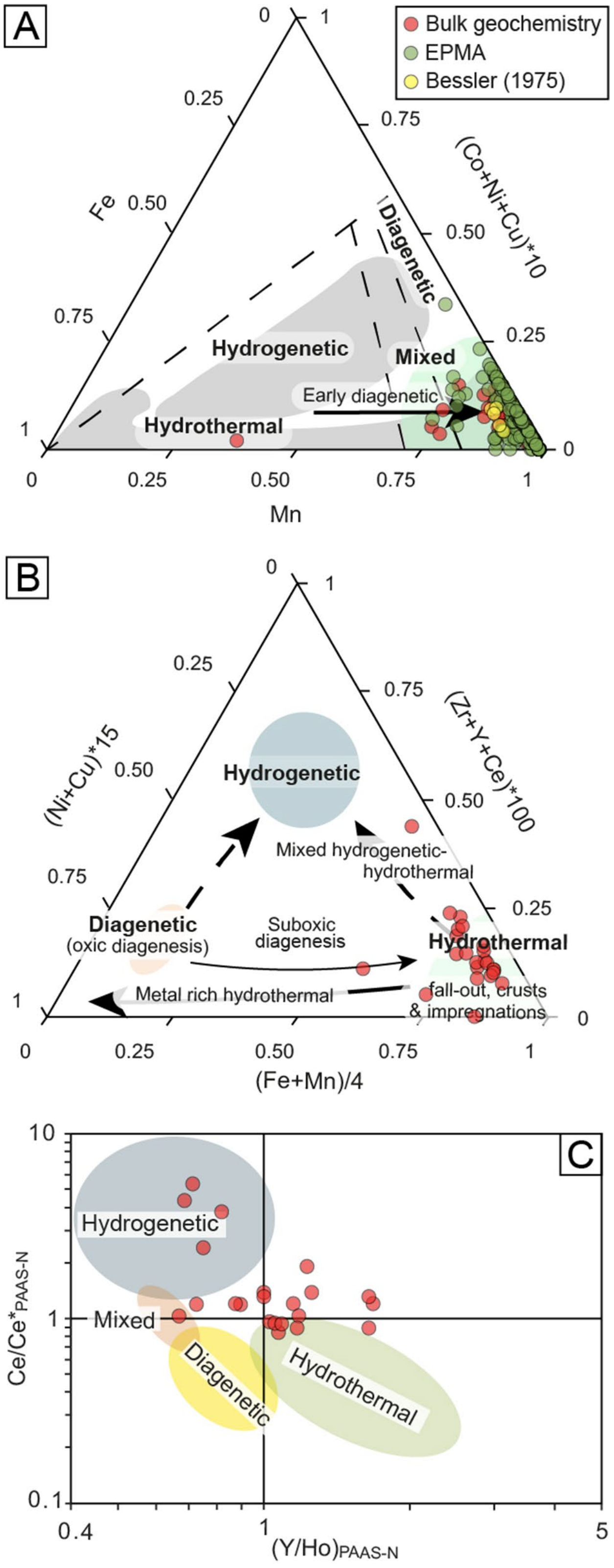

Fig. 12 Genetic discrimination plots for Mn oxides of the East Pisco Basin. **A** Ternary Fe - Mn - (Co + Ni + Cu) × 10 plot with compositional fields after Bonatti et al. (1972) and Zawadzki et al. (2022). EPMA (this study) and bulk geochemistry data (this study) are plotted along with data by Bessler (1975) for comparison. **B** Ternary (Ni + Cu) × 15 - (Fe + Mn)/4 - (Zr + Y + Ce) × 100 plot with compositional fields after Josso et al. (2017). **C** Binary Ce/Ce* vs. $(Y/Ho)_{PAAS\text{-}N}$ genetic discrimination plot for Mn oxides of the East Pisco Basin. $Ce/Ce^* = Ce_{PAAS\text{-}N}/(0.5 \times La_{PAAS\text{-}N} + 0.5 \times Pr_{PAAS\text{-}N})$, where PAAS-N refers to normalization to PAAS using values of McLennan (1989). Compositional fields are after Bau et al. (2014)

hydrogenetic deep-sea nodules. The onshore exposure of Co-rich Mn oxides represents an unexplored metal potential as an alternative to the highly controversial deep seabed mining.

Supplementary Information The online version contains supplementary material available at https://doi.org/10.1007/s00126-025-01364-w.

Acknowledgements The field sampling campaigns were financed by the IRD and µXRF analyses were provided by the Centre of Advanced Mining and Metallurgy (CAMM). We appreciate the technical support by Xavier Llovet (CCiTUB) during the acquisition of EMPA data and by Michelle Dossey (LTU) during the acquisition of µXRF data. We thank Dr. Xolane Reginald Mhlanga and an anonymous reviewer for their constructive comments that helped improve this manuscript. We also acknowledge Associate Editor Alexandre Cabral and Editor-in-Chief Bernd Lehmann for their editorial handling and constructive feedback throughout the review process.

Author contributions Conceptualization: L. Torró, J.A. Proenza, P. Baby. Methodology: I.C. Carcamo-Valencia, L. Torró, L. Ayala, T. Aiglsperger; Formal analysis and investigation: I.C. Carcamo-Valencia, L. Torró, J.S. Ramirez-Briones, T. Aiglsperger; Writing - original draft preparation: I.C. Carcamo-Valencia, L. Torró; Writing - review and editing: all authors; Funding acquisition: L. Torró.

Funding Open access funding provided by Pontificia Universidad Catolica del Peru.
Research was funded by the PE501087814 - 2024 project granted by the Peruvian research agency PROCIENCIA and the FAI- 025 - 2023 project granted by PUCP. In addition, it was logistically supported by the project 2021 SGR 00239 of the Agència de Gestió d'Ajuts Universitaris i de Recerca de Catalunya.

Data availability The data supporting the findings of this study are available within the article and its supplementary materials.

Declarations

Conflict of interest The authors declare no competing interests.

References

Achurra LE, Lacassie JP, Le Roux JP, Marquardt C, Belmar M, Ruiz-del-Solar J, Ishman SE (2009) Manganese nodules in the miocene Bahía Inglesa formation, north-central Chile: petrography, geochemistry, genesis and palaeoceanographic significance. Sediment Geol 217:128–139

Banakar VK, Pattan JN, Mudholkar AV (1997) Palaeoceanographic conditions during the formation of a ferromanganese crust from the Afanasiy-Nikitin seamount, North central Indian Ocean: geochemical evidence. Mar Geol 136:299–315

Baturin GN, Dubinchuk VT (2011) The composition of ferromanganese nodules of the Chukchi and East Siberian seas. Dokl Earth Sci 440:1258–1264

Bau M, Schmidt K, Koschinsky A, Hein JR, Kuhn T, Usui A (2014) Discriminating between different genetic types of marine ferromanganese crusts and nodules based on rare earth elements and yttrium. Chem Geol 60:1709–1725

Benites M, Hein JR, Mizell K, Blackburn T, Jovane L (2020) Genesis and evolution of ferromanganese crusts from the summit of Rio Grande rise, Southwest Atlantic ocean. Minerals 10:349

Bessler E (1975) Sobre la existencia de los nódulos de manganeso en la Formación Pisco. Boletín SGP 50:10–34

Bonatti E, Kraemer T, Rydell H (1972) Classification and genesis of submarine iron-manganese deposits. In: Horn DR (ed) Ferromanganese deposits on the ocean floor, pp 149–166

Böning P, Brumsack HJ, Böttcher ME, Schnetger B, Kriete C, Kallmeyer J, Borchers SL (2004) Geochemistry of Peruvian near-surface sediments. Geochim Cosmochim Acta 68:4429–4451

Boschen RE, Rowden AA, Clark MR, Gardner JPA (2013) Mining of deep-sea seafloor massive sulfides: a review of the deposits, their benthic communities, impacts from mining, regulatory frameworks and management strategies. Ocean Coastal Manag 84:54–67

Bosio G, Gioncada A, Malinverno E, Coletti G, Collareta A, Mariani L, Cavallo A, Bianucci G, Urbina M, Di Celma C (2024) Unraveling marine phosphogenesis along the miocene coast of Peru: origin and sedimentological significance of the Pisco formation phosphorites. Mar Pet Geol 167:106941

Burns RG, Burns VM (1977) Chap. 7 mineralogy. In: Glasby GP (ed) Marine manganese deposits. Elsevier Oceanography Series, Elsevier, Wellington, pp 185–248

Calvert SE, Price NB (1977) Geochemical variation in ferromanganese nodules and associated sediments from the Pacific ocean. Mar Chem 5:43–74

Calvès G, Auguy C, de Lavaissière L, Brusset S, Calderon Y et al (2017) Forearc seafloor unconformities and geology: insight from 3D seismic geomorphology analysis, Peru. Geochem Geophys Geosyst 18:3062–3077

Calvès G, Mix A, Giosan L, Clift PD, Brusset S, Baby P, Vega M (2022) The Nazca drift System– Palaeoceanographic significance of a giant sleeping on the SE Pacific ocean floor. Geol Mag 159:322–336

Casalbore D (2018) Volcanic Islands and seamounts. In: Micallef A, Krastel S, Savini A (eds) Submarine geomorphology. Springer, Berlin, pp 333–347

Chan M (2022) A perspective on concretions: Deciphering diagenesis from Earth to Mars. J Geol Soc Japan 128:445–464

Chan M, Parry W, Bowman J (2000) Diagenetic hematite and manganese oxides and fault-related fluid flow in jurassic sandstones, southeastern Utah. AAPG Bull 84:1281–1310

Clift PD, Pecher I, Kukowski N, Hampel A (2003) Tectonic erosion of the Peruvian forearc, Lima basin, by subduction and Nazca ridge collision. Tectonics 22:1023

Collareta A, Lambert O, Marx FG, de Muizon C, Varas-Malca R, Landini W, Bosio G, Malinverno E, Gariboldi K, Gioncada A, Urbina M, Bianucci G (2021) Vertebrate palaeoecology of the Pisco formation (Miocene, Peru): glimpses into the ancient Humboldt current ecosystem. J Mar Sci Eng 9:1188

Cooke RU, Warren A, Goudie AS (2006) Desert geomorphology. CRC Press, London, pp 307–322

Crouch JK, Bachman SB, Zucker CL (1990) The Peru continental margin: high petroleum potential in a modern fore-arc setting. AAPG Bull 74:5

Cunningham A (2022) Assessing the feasibility of deep-seabed mining of polymetallic nodules in the area of seabed and ocean floor beyond the limits of National jurisdiction, as a method of alleviating supply-side issues for Cobalt to US markets. Min Econ 37:1–20

DeVries TJ, Jud NA (2018) Lithofacies patterns and paleogeography of the miocene Chilcatay and lower Pisco depositional sequences (East Pisco basin, Peru). Boletín SGP 8:124–167

Di Celma C, Malinverno E, Gariboldi K, Gioncada A, Rustichelli A, Pierantoni PP, Landini W, Bosio G, Tinelli C, Bianucci G (2016) Stratigraphic framework of the late miocene to pliocene Pisco formation at Cerro Colorado (Ica desert, Peru). J Maps 12:515–529

Di Celma C, Malinverno E, Bosio G, Collareta A, Gariboldi K, Gioncada A, Molli G, Basso D, Varas-Malca R, Pierantoni P, Villa I, Lambert O, Landini W, Sarti G, Cantalamessa G, Urbina-Schmitt M, Bianucci G (2017) Sequence stratigraphy and paleontology of the upper miocene Pisco formation along the Western side of the lower Ica Valley (Ica desert, Peru). Riv Ital 123:255–273

Di Celma C, Malinverno E, Collareta A, Bosio G, Gariboldi K, Lambert O, Landini W, Pierantoni PP, Gioncada A, Villa IM, Coletti G, De Muizon C, Urbina M, Bianucci G (2018a) Facies analysis, stratigraphy and marine vertebrate assemblage of the lower miocene Chilcatay formation at Ullujaya (Pisco basin, Peru). J Maps 14:257–268

Di Celma C, Malinverno E, Bosio G, Gariboldi K, Collareta A, Gioncada A, Landini W, Pierantoni P, Bianucci G (2018b) Intraformational unconformities as a record of late miocene eustatic falls of sea level in the Pisco formation (southern Peru). J Maps 14:607–619

Di Celma C, Pierantoni PP, Malinverno E, Collareta A, Lambert O, Landini W, Bosio G, Gariboldi K, Gioncada A, De Muizon C, Molli G, Marx FG, Varas-Malca RM, Urbina M, Bianucci G (2019) Allostratigraphy and paleontology of the lower Miocene Chilcatay formation in the Zamaca area, East Pisco basin, Southern Peru. J Maps 15:393–405

Di Celma C, Pierantoni P, Volatili T, Molli G, Mazzoli S, Sarti G, Ciattoni S, Bosio G, Malinverno E, Collareta A, Gariboldi K, Gioncada A, Jablonska D, Landini W, Urbina M, Bianucci G (2022) Towards deciphering the Cenozoic evolution of the East Pisco basin (southern Peru). J Maps 18:1–16

Dunbar RB, Marty RC, Baker PA (1990) Cenozoic marine sedimentation in the Sechura and Pisco basins. Peru Palaeogeogr Palaeoclimatol Palaeoecol 77:235–261

Eisenlohr BN, Tompkins LA, Cathles LM, Barley M, Groves D (1994) Mississippi valley-type deposits: products of brine expulsion by eustatically induced hydrocarbon generation? An example from northwestern Australia. Geology 22:315–318

Espurt N, Baby P, Brusset S, Roddaz M, Hermoza W, Regard V, Antoine P-O, Salas-Gismondi R, Bolaños R (2007) How does the

Nazca ridge subduction influence the modern Amazonian foreland basin? Geology 35:515–518

European Space Agency (2024) Copernicus global digital elevation model. Distrib OpenTopography. https://doi.org/10.5069/G9028PQB. Accessed 29 Aug 2024

García M, Correa J, Maksaev V, Townley B (2020) Potential mineral resources of the Chilean offshore: an overview. Andean Geol 47:1–13

Gariboldi K, Bosio G, Malinverno E, Gioncada A, Di Celma C, Villa I, Urbina M, Bianucci G (2017) Biostratigraphy, geochronology and sedimentation rates of the upper miocene Pisco formation at two important marine vertebrate fossil-bearing sites of Southern Peru. Newsl Stratigr 50:417–444

George SWM, Perez ND, Struble W, Ellis Curry M, Horton BK (2022) Aseismic ridge subduction focused late cenozoic exhumation above the Peruvian flat slab. Earth Planet Sci Lett 600:117754

Gioncada A, Petrini R, Bosio G, Gariboldi K, Collareta A, Malinverno E, Bonaccorsi E, Di Celma C, Pasero M, Urbina M, Bianucci G (2018) Insights into the diagenetic environment of fossil marine vertebrates of the Pisco formation (late miocene, Peru) from mineralogical and Sr-isotope data. J S Am Earth Sci 81:141–152

Glasby GP (1988) Hydrothermal manganese deposits in Island arcs and related to subduction processes: a possible model for genesis. Ore Geol Rev 4:145–153

Glasby GP (2013) Manganese: predominant role of nodules and crusts. In: Schulz HD, Zabel M (eds) Marine geochemistry, 2nd edn. Springer, Berlin, pp 371–427

González FJ, Somoza L, Lunar R, Martínez-Frías J, Martín Rubí JA, Torres T, Ortiz JE, Díaz del Río V, Pinheiro LM, Magalhães VH (2009) Hydrocarbon-derived ferromanganese nodules in carbonate-mud mounds from the Gulf of Cadiz: mud-breccia sediments and clasts as nucleation sites. Mar Geol 261:64–81

González FJ, Somoza L, León R, Medialdea T, de Torres T, Ortiz JE, Lunar R, Martínez-Frías J, Merinero R (2012) Ferromanganese nodules and micro-hardgrounds associated with the Cadiz contourite channel (NE Atlantic): palaeoenvironmental records of fluid venting and bottom currents. Chem Geol 310–311:56–78

Hampel A (2002) The migration history of the Nazca ridge along the Peruvian active margin: a re-evaluation. Earth Planet Sci Lett 203:665–679

Hein JR, Koschinsky A (2014) Deep ocean ferromanganese crusts and nodules. In: Holland HD, Turekian KK (eds) Treatise on geochemistry, 2nd edn. Elsevier, Amsterdam, pp 273–291

Hein JR, Koschinsky A, Halbach P, Manheim FT, Bau M, Kang JK, Lubick N (1997) Iron and manganese oxide mineralization in the Pacific. Geol Soc Lond Spec Publ 119:123–138

Hein JR, Koschinsky A, Bau M, Manheim FT, Kang J-K, Roberts L (2000) Cobalt-rich ferromanganese crusts in the Pacific. In: Cronan DS (ed) Handbook of marine mineral deposits. CRC, Florida, pp 239–279

Hein JR, Mizell K, Koschinsky A, Conrad TA (2013) Deep-ocean mineral deposits as a source of critical metals for high- and green-technology applications: comparison with land-based resources. Ore Geol Rev 51:1–14

Hein JR, Konstantinova N, Mikesell M, Mizell K, Fitzsimmons JN, Lam PJ, Jensen LT, Xiang Y, Gartman A, Cherkashov G, Hutchinson DR, Till CP (2017) Arctic deep water ferromanganese-oxide deposits reflect the unique characteristics of the Arctic ocean. Geochem Geophys Geosyst 18:3771–3800

Hein JR, Koschinsky A, Kuhn T (2020) Deep-ocean polymetallic nodules as a resource for critical materials. Nat Rev Earth Environ 1:158–169

Helmons R, de Wit L, de Stigter H, Spearman J (2022) Dispersion of benthic plumes in deep-sea mining: what lessons can be learned from dredging? Front Earth Sci 10:868701

Hunt JM (1996) Petroleum geochemistry and geology, 2nd edn. W.H. Freeman and Company, New York

Jiang X-D, Sun X-M, Guan Y (2019) Biogenic mineralization in the ferromanganese nodules and crusts from the South China sea. J Asian Earth Sci 171:46–59

Josso P, Pelleter E, Pourret O, Fouquet Y, Etoubleau J, Cheron S, Bollinger C (2017) A new discrimination scheme for oceanic ferromanganese deposits using high field strength and rare earth elements. Ore Geol Rev 87:3–15

Josso P, Parkinson I, Horstwood M, Lusty P, Chenery S, Murton B (2019) Improving confidence in ferromanganese crust age models: a composite geochemical approach. Chem Geol 513:108–119

Katona S, Paulikas D, Stone GS (2022) Ethical opportunities in deep-sea collection of polymetallic nodules from the Clarion-Clipperton zone. Integr Environ Assess Manag 18:634–654

Konstantinova N, Cherkashov G, Hein JR, Mirão J, Dias L, Madureira P, Kuznetsov V, Maksimov F (2017) Composition and characteristics of the ferromanganese crusts from the western Arctic ocean. Ore Geol Rev 87:88–99

Koschinsky A, Hein J, Schmidt K, Alexander B, Bau M (2010) Rare and valuable metals for high-tech applications in marine ferromanganese nodules and crusts: relationships to genetic endmembers. Underwater Mining Institute, Gelendzhik, pp 1–13

Lenstra W, van Helmond N, Zygadlowska O, Zummeren R, Witbaard R, Slomp CP (2022) Sediments as a source of iron, manganese, cobalt and nickel to continental shelf waters (Louisiana, Gulf of Mexico). Front Mar Sci 9:811953

León WR, Torres V (2003) Memoria descriptiva de la revisión y actualización de los cuadrángulos de Punta Grande (29-k), Ica (29–1), Lomitas (30–1), palpa (30-m), San Juan (31-m), Acari (31-n) y Yauca (32-n). Scale 1:100,000. INGEMMET, Lima

León WR, Rosell W, Alemán AM, Torres VR, De la Cruz MO (2008) Estratigrafía, sedimentología y evolución tectónica de la cuenca Pisco Oriental. Boletín INGEMMET 27:1–154

Lusty P, Murton B (2018) Deep-ocean mineral deposits: metal resources and windows into Earth processes. Elements 14:301–306

Lusty P, Hein JR, Josso P (2018) Formation and occurrence of ferromanganese crusts: Earth's storehouse for critical metals. Elements 14:313–318

Macharé J (1987) La marge continentale du Pérou: régimes tectoniques et sédimentaires Cénozoiques de l'avant-arc des Andes Centrales. PhD Thesis, Université de Paris Sud, Paris, France

Macharé J, Ortlieb L (1992) Plio-Quarternary vertical motions and the subduction of the Nazca ridge, central Coast of Peru. Tectonophysics 205:97–108

Malinverno E, Bosio G, Gastaldello ME, Pellegrino L, Bianucci G, Collareta A, Gariboldi K, Urbina M, Villa IM, Di Celma C (2025) The early depositional history of the Pisco formation (Middle to upper miocene, Peru). Newsl Stratigr 58:99–123

McFadden LD, Wells SG, Jercinovich MJ (1987) Influences of eolian and pedogenic processes on the origin and evolution of desert pavements. Geology 15:504–508

McLennan SM (1989) Rare Earth elements in sedimentary rocks: influence of provenance and sedimentary processes. In: Lipin BR, McKay GA (eds) Geochemistry and mineralogy of rare Earth elements. De Gruyter, Berlin, pp 169–200

National Centers for Environmental Information (2022) ETOPO 2022 15 Arc-second global relief model. Accessed 2 March 2025

Ochoa D, Salas-Gismondi R, DeVries T, Baby P, de Muizon C, Sierra A, Barbosa A, Foster D, Quispe K, Cardich J, Gutiérrez D, Perez A, Valqui J, Urbina M, Carré M (2021) Late neogene evolution of the Peruvian margin and its ecosystems: a synthesis from the Sacaco record. Int J Earth Sci (Geol Rundsch) 110:995–1025

Pelleter E, Fouquet Y, Etoubleau J, Cheron S, Labanieh S, Josso P, Bollinger C, Langlade J (2017) Ni-Cu-Co-rich hydrothermal manganese mineralization in the Wallis and futuna back-arc environment (SW Pacific). Ore Geol Rev 87:126–146

Quispe K, Baby P, Calderón Y, Hurtado C, Ramírez L (2018) La Cuenca Pisco: nuevo modelo estructural para una cuenca de antearco Peruana, evidencias de contexto compresivo, desarrollo de la Cordillera de la Costa. XIX Congreso Peruano de Geología. SGP, Lima

Rossello EA, Cossey SPJ, Fernández G (2022) The hydrocarbon potential of the offshore Talara basin, Peru. Andean Geol 49:1–17

Rustichelli A, Di Celma C, Tondi E, Bianucci G (2016) Deformation within the Pisco basin sedimentary record (southern Peru): stratabound orthogonal vein sets and their impact on fault development. J S Am Earth Sci 65:79–100

Shulga N, Abramov S, Klyukina A, Popov V, Dara O, Novichkova E, Lokhov D, Kuleshov V, Osadchiev A, Bubnovskaya R, Morgunova I, Johnston S, Romanova N, Kuklina I, Dubinin A, Kokryatskaya N, Yakushev E, Dale AW, Rozanov A, Shcherbakova V, Kravchishina M (2022) Fast-growing Arctic Fe–Mn deposits from the Kara sea as refuges for cosmopolitan marine microorganisms. Sci Rep 12:21967

Sparenberg O (2019) A historical perspective on deep-sea mining for manganese nodules, 1965–2019. Extr Ind Soc 6:842–854

Thornburg TM, Kulm LD (1981) Sedimentary basins of the Peru continental margin: Structure, stratigraphy, and Cenozoic tectonics from 6°S to 16°S latitude. In: Kulm LD, Dymond J, Dasch EJ, Hussong DM (eds) Nazca Plate: Crustal Formation and Andean Convergence. Geol Soc Am Mem 154:393–422

Toro N, Jeldres RI, Órdenes JA, Robles P, Navarra A (2020) Manganese nodules in Chile, an alternative for the production of Co and Mn in the future— A review. Minerals 10:674

Travis RB, Gonzales G, Pardo A (1976) Hydrocarbon potential of coastal basins of Peru. In: Halbouty MT, Maher JC, Lian HM (eds) Circum-Pacific energy and mineral resources. AAPG Mem 25:331–338

Vereshchagin OS, Perova EN, Brusnitsyn AI, Ershova VB, Khudoley AK, Shilovskikh VV, Molchanova EV (2019) Ferro-manganese nodules from the Kara Sea: mineralogy, geochemistry and genesis. Ore Geol Rev 106:192–204

Viveen W, Schlunegger F (2018) Prolonged extension and subsidence of the Peruvian forearc during the cenozoic. Tectonophysics 730:48–62

Vodyanitskii YN, Vasilév AA, Lesovaya SN, Sataev EF, Sivtsov AV (2004) Formation of manganese oxides in soil. Eurasian Soil Sci 37:572–584

Zawadzki D, Maciąg Ł, Blasco I, González FJ, Wernette B, Marino E, Kozub-Budzyń GA, Piestrzyński A, Wróbel RJ, McCartney K (2022) Geochemistry and mineralogy of ferromanganese crusts from the Western Cocos-Nazca spreading centre. Pac Minerals 12:538

Zhang H, Zhou J, Yuan P, Dong Y, Fan W, Yu X, Lu J (2023) Implication from mineralogical and geochemical characteristics of authigenic micronodules in the Haima cold seeps for Understanding the manganese geochemistry in active seepage. J Geophys Res Oceans 128:1–21

Zhou J, Cai P, Yang C, Liu S, Luo W, Nie X (2022) Geochemical characteristics and genesis of ferromanganese nodules and crusts from the central rift seamounts group of the West Philippine sea. Ore Geol Rev 145:104923